Monthly Notices
of the
ROYAL ASTRONOMICAL SOCIETY

MNRAS **440,** 427–447 (2014)
Advance Access publication 2014 March 11

doi:10.1093/mnras/stu300

A *Herschel* and BIMA study of the sequential star formation near the W 48A H II region★

K. L. J. Rygl,[1,2]† S. Goedhart,[3,4,5] D. Polychroni,[1,6] F. Wyrowski,[4] F. Motte,[7] D. Elia,[1] Q. Nguyen-Luong,[8] P. Didelon,[7] M. Pestalozzi,[1] M. Benedettini,[1] S. Molinari,[1] Ph. André,[7] C. Fallscheer,[9,10] A. Gibb,[11] A. M. di Giorgio,[1] T. Hill,[7,12] V. Könyves,[7,13] A. Marston,[14] S. Pezzuto,[1] A. Rivera-Ingraham,[15,16] E. Schisano,[17] N. Schneider,[18] L. Spinoglio,[1] D. Ward-Thompson[19] and G. J. White[20,21]

Affiliations are listed at the end of the paper

Accepted 2014 February 12. Received 2014 February 12; in original form 2013 September 6

ABSTRACT

We present the results of *Herschel* HOBYS (*Herschel* imaging survey of OB Young Stellar objects) photometric mapping combined with Berkeley Illinois Maryland Association (BIMA) observations and additional archival data, and perform an in-depth study of the evolutionary phases of the star-forming clumps in W 48A and their surroundings. Age estimates for the compact sources were derived from bolometric luminosities and envelope masses, which were obtained from the dust continuum emission, and agree within an order of magnitude with age estimates from molecular line and radio data. The clumps in W 48A are linearly aligned by age (east-old to west-young): we find a ultra-compact (UC) H II region, a young stellar object (YSO) with class II methanol maser emission, a YSO with a massive outflow and finally the NH_2D prestellar cores from Pillai et al. This remarkable positioning reflects the (star) formation history of the region. We find that it is unlikely that the star formation in the W 48A molecular cloud was triggered by the UC H II region and discuss the Aquila supershell expansion as a major influence on the evolution of W 48A. We conclude that the combination of *Herschel* continuum data with interferometric molecular line and radio continuum data is important to derive trustworthy age estimates and interpret the origin of large-scale structures through kinematic information.

Key words: stars: formation – ISM: clouds – dust, extinction – H II regions – ISM: individual objects: W 48A – ISM: molecules.

1 INTRODUCTION

Sequential star formation in the structure of OB associations was noted already in 1960s (e.g. Blaauw 1964; Elmegreen & Lada 1977 and references therein). More recently, also on smaller scales stellar age gradients are observed, such as for bright-rimmed clouds (see e.g. White et al. 1997; Thompson et al. 2004; Matsuyanagi et al. 2006; Ogura et al. 2007) and for star formation on the borders of H II regions (e.g. Deharveng, Zavagno & Caplan 2005; Zavagno et al. 2010b). Evidence for sequential star formation should also be present during the earliest stages of star formation. Molecular clouds containing star-forming objects at various stages of evolution are commonly observed: the *Spitzer* study of Qiu et al. (2008) shows the distributions of the various evolutionary classes of young stellar objects (YSOs) within one cloud; and molecular line studies of infrared-dark and high-extinction clouds find collapsing dense infrared-dark cores next to active infrared-bright star-forming ones (see, e.g., Palau et al. 2010; Rygl et al. 2010, 2013). More recently, a few *Herschel* HOBYS (*Herschel* imaging survey of OB Young Stellar objects) studies have investigated star formation near OB clusters and bubble-shaped objects in view of triggered star formation (e.g., RCW 120: Zavagno et al. 2010a; Rosette: Schneider et al. 2010, 2012; Tremblin et al. 2014; W5-E: Deharveng et al.

★*Herschel* is an ESA space observatory with science instruments provided by European-led Principal Investigator consortia and with important participation from NASA. This work is partially based on observations carried out with the IRAM 30 m Telescope. IRAM is supported by INSU/CNRS (France), MPG (Germany) and IGN (Spain).

†E-mail: krygl@rssd.esa.int

2012; W 3: Rivera-Ingraham et al. 2013; NGC 7538: Fallscheer et al. 2013). It has not been proven yet whether all sequential star formation is the consequence of triggering, and evidence to the contrary has been found for the Rosette region through observations (Schneider et al. 2012; Cambrésy et al. 2013) and simulations (e.g. Dale & Bonnell 2011, 2012). Determining age gradients across a star-forming region can give insight into the star formation history by which one can assess the possibility of triggering and its size scale. In this paper, we analysed the age gradient in W 48A, a region with a trustworthy distance and various stages of star formation, tapping into new dust continuum and spectral line data as well as archival data.

W 48A is part of a group of H II regions (Onello et al. 1994) located at a distance of 3.27 ± 0.49 kpc (maser parallax; Zhang et al. 2009a) about 1.°7 below the Galactic plane. Arthur & Hoare (2006) describe it as a 'classical' champagne flow plus stellar wind ultra-compact (UC) H II region where the photodissociation region (PDR) is moving with 2.5 km s^{-1} into the molecular cloud (Roshi et al. 2005). The star-forming region W 48A is known to host several different stages of high-mass star formation: a UC H II region (G 35.20−1.74; Wood & Churchwell 1989) embedded in a larger, almost 2 arcmin × 2 arcmin, cometary part (Wood & Churchwell 1989; Kurtz, Churchwell & Wood 1994; Onello et al. 1994; Roshi et al. 2005) extending to the south-east, a methanol maser-emitting YSO (Minier, Booth & Conway 2000) and some recently discovered prestellar cores containing cold and deuterated molecules (Pillai et al. 2011).

W 48A was observed with the *Herschel* Space Observatory (Pilbratt et al. 2010) at 70–500 μm under the HOBYS programme (Motte et al. 2010) as a part of a larger map of the W 48 molecular cloud complex (see the entire *Herschel* maps in Nguyen Luong et al. 2011). These observations are a powerful tool to visualize the large-scale structure of the cold (160–500 μm) and warm (70 μm) dust emission. *Herschel*'s wavelength coverage is ideal to sample the peak of the spectral energy distribution (SED) of cold and warm (10–30 K) dusty prestellar material and envelopes around YSOs to obtain their temperatures and masses. Since high-mass stars form deeply embedded in their natal cloud, the bulk of their emission is absorbed by the surrounding envelope and is re-emitted in the infrared to mm regime. The infrared luminosity is therefore important for obtaining the bolometric luminosity and determining the spectral type of the embedded star. With the help of a luminosity–mass (L/M) diagram (Saraceno et al. 1996; Molinari et al. 2008; Elia et al. 2010; Hennemann et al. 2010), one can characterize the evolutionary stage of the YSO through its bolometric luminosity and envelope mass.

The *Herschel* maps were combined with BIMA+IRAM 30 m interferometric molecular line imaging to provide a sub-arcsecond resolution view into the star-forming region, down to size scales of ∼1000 au, and with several archival data sets from the Very Large Array (VLA) and James Clerk Maxwell Telescope (JCMT). Molecular line and radio continuum data offer an alternative YSO age estimation to that from the L/M diagram. In particular, we used the NH_3 (1, 1) and (2, 2) lines to trace the earlier stages of star formation, the CO (3–2) line to find evidence of outflows, and the CH_3CN (6–5), $K = 1, 2, 3, 4$, transitions and 107 GHz methanol masers to trace more the hot and dense gas around YSOs. Furthermore, we used the molecular line data to obtain kinematical information: methanol masers for the small-scale kinematics around the star-forming objects and $C^{18}O$ (1–0) data for the large-scale kinematics.

2 OBSERVATIONS AND DATA REDUCTION

In Table 1, we give an overview of all the observed continuum wavelengths and molecular transitions, including the observatory, beam sizes, map sizes and the rms image noise. The observations are presented individually, per observatory, in the following subsections.

2.1 *Herschel* observations and data reduction

The *Herschel* 70, 160, 250, 350 and 500 μm observations of W 48 (ObsIDs: 1342204856 and −7) were carried out in 2010 September using the Photodetector Array Camera and Spectrometer (PACS; Poglitsch et al. 2010) and the Spectral and Photometric Imaging Receiver (SPIRE; Griffin et al. 2010) instruments in parallel mode at a scanning speed of 20 arcsec s^{-1}. The instruments scanned the W 48 field in two perpendicular directions, so that each part of the sky was sampled by several bolometer units. The resulting area observed by both PACS and SPIRE covered 2.°5 × 2.°5, including a part of the Galactic plane and reaching slightly beyond the Galactic latitude of −2.°1. After exporting the level-0.5 data from HIPE v 9.0.0 (Ott 2010), the data were reduced with the UNIMAP mapmaker v 5.4.4 (for details, see Traficante et al. 2011 and Piazzo et al. 2012). Maps reduced with UNIMAP are of equivalent quality as those produced with SCANAMORPHOS (Roussel 2013) and HIPE, the general mapmakers used in the HOBYS programme (e.g. see Nguyen Luong et al. 2011). The maps were astrometrically aligned with the 24 μm MIPSGAL (Carey et al. 2009) data. Absolute (extended) flux calibration of the *Herschel* data was done by applying the offsets obtained from the comparison of extended emission from *Herschel* data with that from *Planck* and *IRAS* data, as described in Bernard et al. (2010), yielding a 20 per cent flux uncertainty. Bright emission

Table 1. Summary of the observed/archival continuum and spectral line data.

Line	$\nu/\lambda^{a,b}$ (GHz/μm)	Observatory	Beam Size^c ($''$, $''$, $^\circ$)	Map Size	$\sigma_{\rm image}$ (mJy beam^{-1})
NH_3 (1, 1)	23.694	VLA	8.8,7.0,42.3	2′ × 2′	1.2
NH_3 (2, 2)	23.722	VLA	8.8,7.0,42.3	2′ × 2′	1.2
CH_3OH (3_1–4_0)	107.014	BIMA	0.57, 0.24, 45.9	1.′6 × 1.′6	250
$C^{18}O$ (1–0)	109.782	B+30 m	5.2, 4.1, 1.4	1.′6 × 1.′6	22
$C^{18}O$ (1–0)	109.782	IRAM30 m	21.8	2.′9 × 2.′9	120
^{13}CO (1–0)	110.198	BIMA	4.9, 4.0, 2.1	1.′6 × 1.′6	45
CH_3CN (6–5)^d	110.383	BIMA	4.7, 3.9, 4.9	1.′6 × 1.′6	65
CO (3–2)	345.796	JCMT	14	6.′5 × 6.′5	12 × 10^3
Continuum	2800^b	BIMA	2.3, 1.9, 3.5	1.′6 × 1.′6	3.0
Continuum	1250^b	IRAM30 m	11	0.°3 × 0.°3^e	19
Continuum	850^b	JCMT	22.9^f	8.′8 × 8.′8	90
Continuum	500^b	*Herschel*	36	2.°5 × 2.°5	110
Continuum	450^b	JCMT	17.0^f	8.′8 × 8.′8	1.5 × 10^3
Continuum	350^b	*Herschel*	25	2.°5 × 2.°5	69
Continuum	250^b	*Herschel*	18	2.°5 × 2.°5	110
Continuum	160^b	*Herschel*	12	2.°5 × 2.°5	34
Continuum	70^b	*Herschel*	6	2.°5 × 2.°5	16

Notes. Columns are (from left to right): molecular species and transition; frequency or wavelength; observatory; (synthesized) beam size; maps size or field of view (primary beam); rms image noise. ^{a}Molecular line frequencies are from the JPL molecular data base (Pickett et al. 1998). ^{b}For the dust continuum, the wavelengths (in μm) are given rather than the frequencies. ^{c}For single-dish maps, the beam is assumed to be circular. 10 arcsec corresponds to 0.16 pc at 3.27 kpc. ^{d}Covering the $K = 0$, 1, 2, 3 and 4 components. ^{e}The 1.2 mm map is a part of a larger map of 1.°5 × 1.°3, which was not fully covered. ^{f}Effective beam sizes as quoted in Di Francesco et al. (2008) rather than the nominal beam sizes.

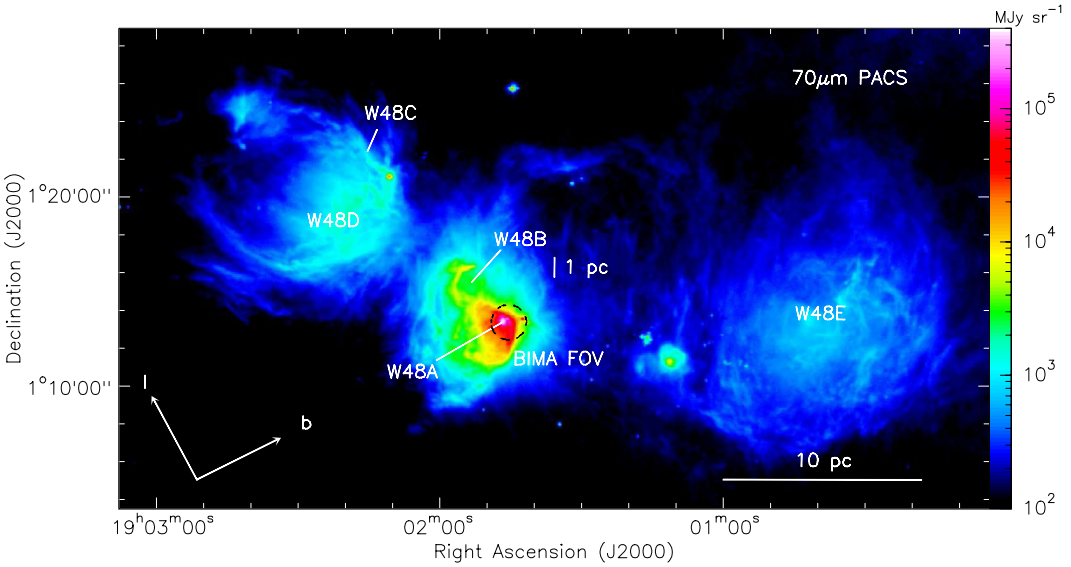

Figure 1. *Herschel* 70 μm map of the W 48 H II regions. The field of view (FOV) of the BIMA observations is indicated. The orientation of the Galactic coordinates is shown in the bottom-left corner.

of the W 48A UC H II region caused three pixels to be saturated in the SPIRE 250 μm map. To correct for this, W 48A was observed again (ObsID: 1342244164) on 2012 December 4 with SPIRE in the small map mode (12 arcmin × 15 arcmin, cross scan at the 30 arcsec s^{-1} scanning speed) and the saturated pixels were replaced. No saturation problems were encountered at the other wavelengths. We estimated the rms image noise (Table 1) for each map from the mean flux of the pixels in a relatively blank region. The conversion from Jy beam^{-1} to MJy sr^{-1} is Jy beam^{-1} × 10^{-6} × $(\frac{\theta}{206\,265})^2$ × $\frac{\pi}{4\ln 2}$ = MJy sr^{-1}, where θ is the beam full width at half-maximum (FWHM) in arcseconds. Fig. 1 gives an overview of the W 48 UC H II regions (using the naming convention from Onello et al. 1994). Maps of W 48A at all *Herschel* wavelengths are shown in Fig. 2.

2.2 BIMA observations and data reduction

Observations were made using the Berkeley Illinois Maryland Association (BIMA) interferometer at 110 GHz (2.8 mm). All antenna configurations, i.e. A, B, C and D configurations, were used in order to achieve high dynamic range images. The nominal beam sizes at 3 mm were 0.4 arcsec for the A configuration, 2 arcsec for the B configuration, 6 arcsec for the C configuration and 18 arcsec for the D configuration. The dates of the observations were 2000 December 18, 25 and 31 (A configuration); 2003 February 1 (B configuration); 2000 July 14 (C configuration); 2000 May 23 (D configuration). The continuum phase calibrator used was J1751+096. The pointing centre of the array was 19^h 01^m 45^s.448 +01° 13′ 21″.49 (J2000). Due to the instability of the atmosphere at ∼3 mm, the observations using the extended A-array configuration were done in fast switching mode. Fig. 2 shows the high dynamic range 2.8 mm continuum map of W 48A. Our BIMA continuum appears different from that measured at 3.5 mm with the Plateau de Bure Interferometer (PdBI) by Pillai et al. (2011), because our BIMA observations are a factor of ∼4 less sensitive plus our pointing centre was ∼50 arcsec east of that used in the observations of Pillai et al. (2011), decreasing our sensitivity in the western part of W48 A, which was the objective of their PdBI observations. The pointing accuracy ($\sigma_{\rm poi}$) can be estimated following Reid et al. (1988) by

$$\sigma_{\rm poi} = \left(\frac{4}{\pi}\right)^{0.25} \frac{\theta}{\sqrt{8\ln 2}} \frac{1}{\rm SNR}, \quad (1)$$

where θ is the synthesized beam FWHM in arcseconds and SNR is the maximal flux divided by the rms noise level. For the BIMA continuum map, the pointing accuracy was 0.02 arcsec.

Twelve spectral windows were used, targeting the UC H II region continuum emission as well as line emission from the 107 GHz CH_3OH (3_1–4_0, A^+) masers in the lower sideband and CH_3CN (6–5), $K = 0, 1, 2, 3, 4$ levels, $C^{18}O$ (1–0) and ^{13}CO (1–0) transitions in the upper sideband. The channel separations for the lines observed with BIMA are 1.06 km s^{-1} for the CH_3CN lines, 8.50 km s^{-1} for the ^{13}CO line, and 0.27 km s^{-1} for the $C^{18}O$ line and 107 GHz methanol maser emission. For the $C^{18}O$ line, we obtained also a single-dish data cube (see Section 2.3) to have the zero-spacings for complementing the interferometric BIMA data.

Data reduction was carried out with the MIRIAD package (Sault, Teuben & Wright 1995). A phase-delay correction for the lower sideband was found using the continuum phase calibrator. The A-array observations were used to generate a model of the methanol maser. This model was used to self-calibrate the maser observations at all array configurations. The self-calibration solution was then applied to all spectral windows. The upper sideband observations still had a residual phase error so an additional phase calibration was done on the continuum calibrator in the upper sideband. The final beam sizes of each map are reported in Table 1.

2.3 IRAM 30 m data

$C^{18}O$ (1–0) line observations of W 48A were carried out in two observing blocks in 2003 March under project number 138-02 at the Institut de Radioastronomie Millimétrique (IRAM) 30m telescope. We used the old ABCD receivers in combination with the Versatile Spectrometer Assembly (VESPA) backend using a bandwidth of 40 mHz and a channel spacing of 0.22 km s^{-1}. During the observations, a pointing check was performed approximately every hour on quasar J1749+096, depending on the weather conditions,

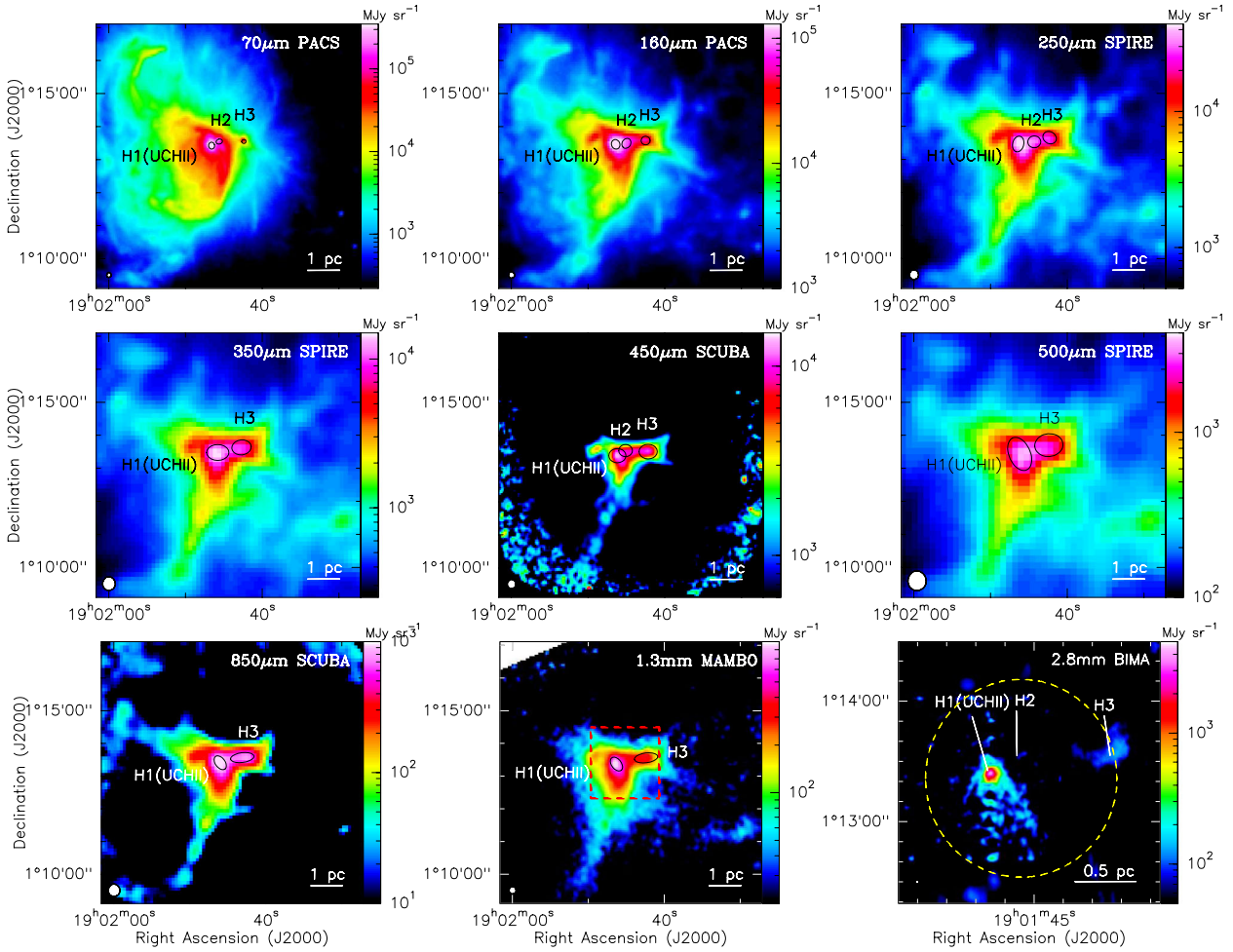

Figure 2. PACS, SPIRE, SCUBA, MAMBO and BIMA continuum images of W 48A. All map units are MJy sr^{-1}. Beam sizes are shown in the bottom-left corner of each map. The MAMBO map has been smoothed to have a 13 arcsec beam. All maps have the same dimension, except for the BIMA image, which is smaller. The red dashed box in the MAMBO map shows the area of the BIMA image. The BIMA field of view is indicated by a yellow dashed circle. For each map, we show with ellipses clumps H-1, H-2 and H-3 (see Table 2) as obtained through CUTEX (see Section 3.1.1) for that map, except for the BIMA map, where the location of the clumps is given for the reader's convenience and does not refer to a source detection.

which were average in block 1 to good in block 2. The precipitable water vapour (pwv) in block 1 was 6 mm and system temperatures ranged between 139 and 507 K. For the second observing block, the pwv was 3–4 mm with system temperatures of 191–292 K. A focus check was performed on Mars at the beginning of each observing block. The observed output counts were calibrated to antenna temperatures, T_A^*, using the standard chopper-wheel technique (Kutner & Ulich 1981), and converted to main beam brightness temperatures by multiplying by the ratio of the forward efficiency (97 per cent) to the main beam efficiency (54 per cent) at 110 GHz.

The C^{18}O single-dish data were used as the zero-spacing for the C^{18}O interferometric BIMA data. An image cube was made of the BIMA data using maximum entropy deconvolution, excluding A-array data. Care had to be taken to use an image size smaller than the single-dish image in order to avoid regridding artefacts at the edge of the smaller single-dish image. The single-dish image was then regridded to match the BIMA image. A joint maximum entropy deconvolution of the BIMA and IRAM 30 m data was done with MIRIAD's MOSMEM task using rms scaling factors of 1.5 and 2.5 for the BIMA and IRAM 30 m data, respectively.

Continuum data were obtained in 2008 January using the Max-Planck Millimeter Bolometer Array (MAMBO-2; Kreysa et al. 1998) under project number 024-07. MAMBO-2 is a 117-pixel array (array size 4 arcmin) that observes at 1.25 mm (240 GHz). While these observations covered a large area ($\sim 1\overset{\circ}{.}5 \times 1\overset{\circ}{.}3$), in this paper we use only the part covering the W 48A UC H II region. The MAMBO observations were performed in fast scanning mode during rough weather conditions (typical opacities at 225 GHz varied between 0.2 and 0.4). Before each W 48 map segment, a pointing was carried out on the nearby G034.26+00.15 H II region. Calibration was performed using the same H II region, yielding accuracies between 10 and 30 per cent. Data reduction was done following the standard pipeline in MOPSIC written by R. Zylka. The entire MAMBO map is shown in Fig. A1, while the part covering W48 A is shown in Fig. 2.

2.4 Archival data

2.4.1 JCMT data

The 450 and 850 μm continuum data from the fundamental catalogue of Di Francesco et al. (2008) and Jenness et al. (2011) were taken with the Submillimetre Common User Bolometer Array (SCUBA; Holland et al. 1999) mounted at the JCMT. The

Table 2. Cold dust continuum properties of W 48A clumps and cores.

Object	RA (J2000) ($^h:^m:^s$)	Dec. (J2000) ($^\circ:':''$)	R^a_{160} (pc)	R_{CH_3CN} (pc)	M_{env} ($M_\odot$)	T_{dust} (K)	β	L_{bol} ($L_\odot$)	Age (10^5 yr)	Age range (10^5 yr)
Clump H-1	19:01:46.6	01:13:25	0.10		720 ± 250	37 ± 4	1.5 ± 0.1	77200 ± 15000	7.5	2–13
Clump H-2	19:01:45.7	01:13:33	0.11		240 ± 60	27 ± 4	2.0[b]	11200 ± 500	15.1	2.4–12
Clump H-3	19:01:42.4	01:13:33	0.10		1100 ± 600	21 ± 4	1.7 ± 0.2	4000 ± 1500	1.2	0.9–1.5
Core H-2a	19:01:45.5	01:13:33		0.05	170 ± 30	27 ± 9	2.0[b]	8000 ± 1000	8.0	6.8–9.5
Core H-3b	19:01:42.3	01:13:33		0.08	420 ± 200	19 ± 4	1.9 ± 0.3	2700 ± 600	1.5	1.0–2.0

Notes. Columns are (from left to right): object name; positions of clumps (continuum) and cores (CH_3CN); clump radius at 160 μm; radius of CH_3CN core; envelope mass; dust temperature; grain emissivity parameter; bolometric luminosity; L/M-based average age estimation and the range of ages from the two nearest star formation tracks. [a]Radius is the half of the FWHM of the Gaussian fit performed with CUTEX on the 160 μm map and deconvolved from the beam at 160 μm, 12 arcsec. [b]For clump H-2 and core H-2a, the emissivity index β was fixed at 2.0 because the SEDs had no millimetric data points.

effective beams of the 450 and 850 μm SCUBA data were 17 and 22.9 arcsec (Di Francesco et al. 2008), respectively. Fig. 2 shows the two SCUBA maps of W 48A.

In addition to the continuum data, we downloaded raw CO (3–2) spectral line data of W 48A from the JCMT/ACSIS archive. These data were obtained on 2008 April 21 with the Heterodyne Array Receiver Program (HARP) array under project name M08AU19 (PI: S. L. Lumdsen). HARP is a 16-pixel camera (4 × 4 array) with a footprint on the sky of 2 arcmin. We reduced the HARP data using the JCMT STARLINK ORAC-DR pipeline (Cavanagh et al. 2008). The CO data have a channel spacing of 0.42 km s^{-1}. The total on-source observation time was ∼20 min. The observations were carried out in raster mode using a scan velocity of 7.3 arcsec s^{-1}. The final map had 6.5 arcmin × 6.5 arcmin dimensions, centred on the W 48A UC H II region, at $19^h01^m46\overset{s}{.}7$ +01° 13′ 18″.

2.4.2 *VLA data*

We collected NH_3 (1,1) and (2,2) data from the NRAO's[1] VLA data archive. The ammonia lines were observed under programme AM652 (PI: V. Minier) on 2000 August 3 with the VLA in D configuration. W 48 was observed in dual polarization using two 64 channel intermediate frequency (IF) bands, with the first IF centred on NH_3 (1,1) and the other on NH_3 (2,2). The channel width of the two maps was ∼0.62 km s^{-1}, enough to resolve the hyperfine structure of the NH_3 (1,1) line. The hyperfine structure of NH_3(2,2) is wider (see Barrett, Ho & Myers 1977) than that of NH_3(1,1): the inner satellites were located at the border of the observed band and could not be detected. The total on-source integration time was ∼50 min. The VLA ammonia maps were obtained in one pointing centred on $19^h01^m45\overset{s}{.}5$ +01° 13′ 28″, thus covering the entire W 48A region in the primary beam (FWHM ∼2 arcmin, Table 1). The data reduction was done following the standard AIPS (Greisen 2003) and MIRIAD (Sault et al. 1995) routines.

3 RESULTS AND ANALYSIS OF COMPACT OBJECTS

3.1 Cold dust emission from *Herschel* to IRAM 30 m

3.1.1 *Source extraction and SED fitting*

W 48A's compact source detection and extraction was performed with the Curvature Threshold Extractor (CUTEX; Molinari et al. 2011) in each of the five *Herschel* bands, the SCUBA 450 and 850 μm map, and the MAMBO 1.3 mm map. CUTEX uses the second derivative of the emission map to obtain source locations, and then derives the source parameters, such as their size, peak flux, etc., through two-dimensional Gaussian fitting (see Molinari et al. 2011 for more details). We used a curvature threshold of 1.5, and required the source detection to have a signal-to-noise level higher than 3.0. Sources across the eight bands were associated according to their positions, requiring the positional distance to be within the radius of the FWHM beam size at the longer wavelength (see Elia et al. 2010 for more details). The deconvolved sizes of the compact sources were found to increase with wavelength, which is commonly found in previous *Herschel* studies (see e.g. Nguyen Luong et al. 2011; Giannini et al. 2012) for sources embedded within a large-scale emitting structure such as a low-density envelope. In Table 1, one can see that the beam size of the *Herschel* bands increases with wavelength. Therefore, at longer wavelengths the star-forming clump is more confused with its lower density envelope, which causes its size and intensity to be overestimated. One can correct for this by assuming a density profile for the dust envelope.

Following the method introduced by Motte et al. (2010), we assumed a density profile of $n \propto r^{-2}$, and scaled the intensity of the SPIRE 250, 350, 500 μm and SCUBA 850 μm sources by the ratio of the deconvolved source size at 160 μm and that at 250, 350, 500 and 850 μm, respectively (see Nguyen Luong et al. 2011 for a detailed explanation of the flux scaling). In this scaling, we assume that the emission between 160 and 850 μm is optically thin and emanates from the same volume of gas. From previous SED analysis of *Herschel* sources (e.g. Giannini et al. 2012), these assumptions appear valid. The 450 μm point source fluxes were not flux-scaled since the sources were unresolved within the 17 arcsec beam.

We found three compact sources in the W 48A region, clumps H-1, H-2 and H-3. Clump H-1 was detected in all wavelengths, from 70 μm down to 2.8 mm (and to cm wavelengths), clump H-2 was not detectable longwards of 450 μm and clump H-3 was detected down to 1.3 mm. Using the convention of Henning (2008), objects with radii ≥ 0.1 pc are called clumps, while objects with radii < 0.1 pc are called cores (see Table 2 for the radii). CUTEX results of these clumps at each wavelength are shown by ellipses in Fig. 2. The clumps were found to be well separated from each other, and did not suffer from blending at the detected wavelengths. The only exception is clump H-2 at 350 and 500 μm: this clump was not detected at these wavelengths and it is possible that its emission was confused with that of clump H-1. Clump H-1 coincides with the W 48A UC H II region (G 35.20−1.74), and is the only one with a previous *IRAS* detection (Wood & Churchwell 1989). Clump H-2 is spatially coincident with the location of several maser species: water masers

[1] The National Radio Astronomy Observatory is a facility of the National Science Foundation operated under cooperative agreement by Associated Universities, Inc.

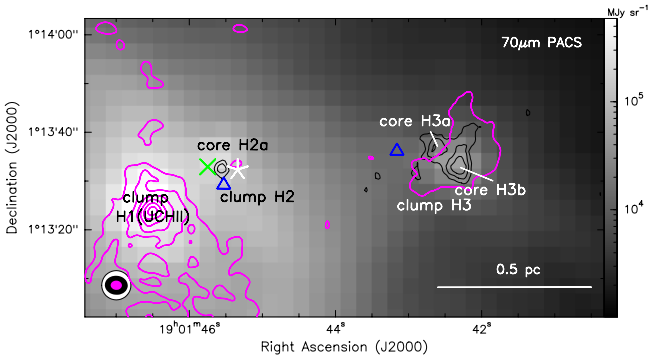

Figure 3. 70 μm PACS map overlaid with black contours for the total intensity CH_3CN map integrated over the K=0 and K=1 emission lines showing the locations of the CH_3CN cores, and magenta contours for the 2.8 mm BIMA continuum. The beam sizes of the 70 μm (white), CH_3CN (black) and the 2.8 mm (magenta) maps are indicated in the bottom-left corner. The CH_3CN contours start at 3σ (0.06 Jy beam^{-1} km s^{-1}) and range up to 1.2 Jy beam^{-1} km s^{-1} with increments of 0.02 Jy beam^{-1} km s^{-1}. The 2.8 mm contours start at 3σ (9mJy) with steps by a factor of 3. Marked are the maser species observed: hydroxyl masers (green cross; Caswell 2001), methanol (white star; this work) and water masers (blue triangle; Hofner & Churchwell 1996). The masers around core H-2a have been offset from the core centre artificially. The locations of clumps and cores are indicated on the map.

(Hofner & Churchwell 1996), hydroxyl masers (Caswell 2001) and methanol masers (e.g. Minier et al. 2000; Val'tts & Lyubchenko 2002). Clump H-3 coincides with the 850 μm continuum source W 48W (Curran et al. 2004) and a water maser detection (Hofner & Churchwell 1996).

Table 2 gives the clump (and core) positions. It is known that clumps can fragment into smaller components (cores) at higher angular resolutions (Zhang et al. 2009b; Bontemps et al. 2010; Hennemann et al. 2010; Wang et al. 2011; Palau et al. 2013). Using our interferometric CH_3CN data (see Section 3.3), we found that clump H-2 contains a more compact core, which we name core H-2a, and that clump H-3 fragments into two CH_3CN cores, H-3a and H-3b (see Fig. 3). Using the same density profile, $n \propto r^{-2}$, we rescaled the continuum fluxes to the sizes of CH_3CN cores (see Table 2). The fluxes of clump H-3 were rescaled to the size of core H-3b rather than core H-3a, since the location of core H-3b coincides with the centre of clump H-3, while H-3a does not (Fig. 3). Moreover, towards core H-3b we detected extended 2.8 mm continuum emission (BIMA), while none was found towards core H-3a. Also in the PdBI data of Pillai et al. (2011), core H-3a does not coincide with any compact continuum emission, while core H-3b coincides with their PdBI mm1 core. Due to the complete absence of continuum emission towards core H-3a, we do *not* consider it as a star-forming object, and we attribute all the continuum emission to H-3b.

To obtain masses and temperatures, we fitted a single-temperature modified blackbody function to all the continuum fluxes assuming flux uncertainties of 20 per cent. The grain emissivity parameter β was allowed to vary between 1 and 2.5 (Sadavoy et al. 2013) for clumps/cores with ancillary millimetric data and kept constant at 2.0 otherwise. Errors in temperature, mass, β and luminosity were estimated by varying the continuum fluxes (±20 per cent) and estimating how much these quantities changed. The clump and core SEDs are shown in Fig. 4 with the best modified blackbody fit, while the resulting masses, temperatures and β's are given in Table 2. From the fit to the SED of clumps H-1 and H-3 (Fig. 4), one can see that the scaled *Herschel* and JCMT (850 μm) fluxes match

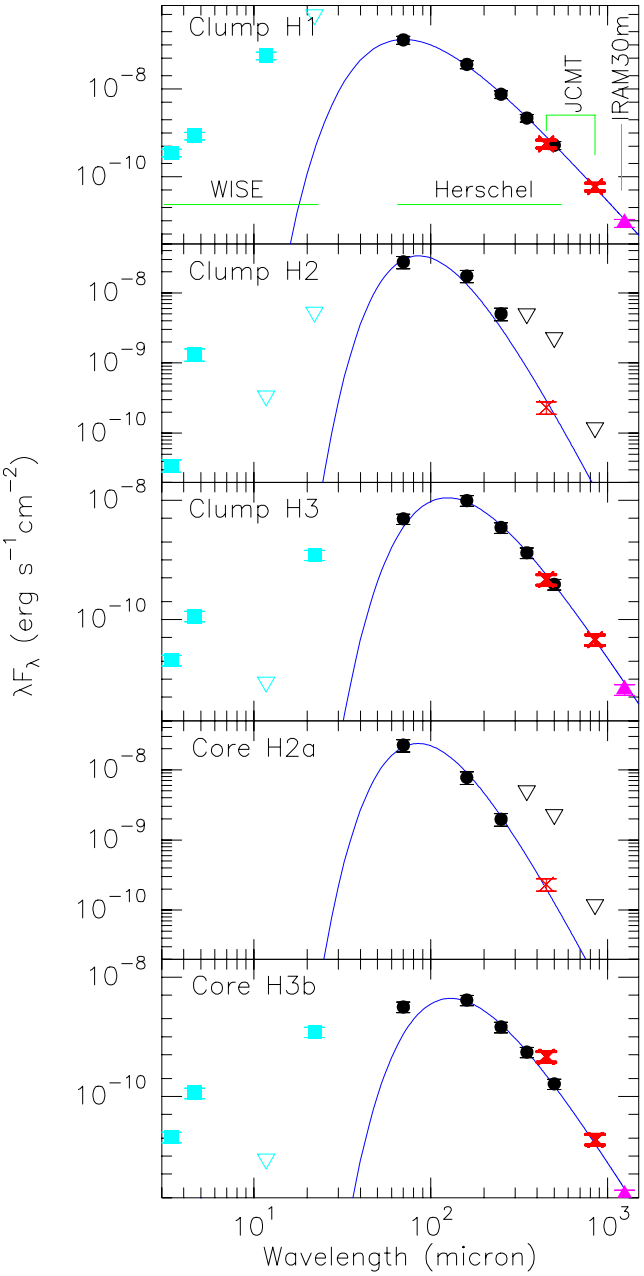

Figure 4. SEDs of clumps H-1, H-2 and H-3 and cores H-2a and H-3b. Downward facing triangles indicate 3σ upper limits. The grey-body fit to the cold dust component is shown by a blue line. The estimated masses, temperatures, dust emissivity and bolometric luminosities are listed in Table 2. Data points from the various observatories are colour coded: cyan squares for *WISE*, black filled dots for *Herschel*, red crosses for JCMT and violet filled triangles for IRAM 30 m.

well with unscaled the IRAM 30 m data points justifying the flux scaling on the 160 μm size. Thanks to the SCUBA 450 μm data, we could confine the clump H-2/core H-2a SED and obtain relatively good estimates of masses, temperatures and luminosities. However, because this source was lacking millimetre detections, we kept β = 2.0. We find that clumps H-1 and H-2 are warmer and less massive than clump H-3. Rescaling the clump fluxes with the core sizes did not significantly affect the temperatures, but strongly reduced the envelope masses.

3.1.2 Millimetre emission and free–free contamination

Close to H II regions, free–free emission will be present in addition to thermal dust emission. Free–free emission dominates at centimetre frequencies, and contributes to the thermal emission at millimetre and submillimetre wavelengths. Using the radio free–free emission of the W 48A UC H II region reported by Roshi et al. (2005), we extrapolated the free–free contribution at 850 μm (10 per cent – 1.76 Jy) and 1.2 mm (32 per cent – 1.80 Jy) and corrected the clump H-1 fluxes at these wavelengths, which were used for SED fitting, accordingly. In the 2.8 mm map (Fig. 2), the UC H II region is clearly visible as a bright source with some weak extended emission flowing southwards, which is thought to be associated with the compact centimetre component identified by Kurtz & Franco (2002). Towards clump H-2, we found very weak 2.8 mm emission, at about a 2.5σ level given the image noise of 3 mJy beam^{-1}, not significant enough for our selection criteria. The millimetre emission towards clump H-3 is a bit stronger (about 3σ–4σ) and its shape correlates well the cold *Herschel* dust continuum emission (Fig. 2), suggesting that it is real. The extrapolation of the modified blackbody fit performed on the extended emission in the *Herschel* bands would predict about 16 mJy per 11.5 arcsec pixel, while the BIMA map contains about 20 mJy per 11.5 arcsec pixel in that area. We conclude that most of the extended 2.8 mm flux around clump H-3 originates in thermal dust emission.

3.1.3 Bolometric luminosities and age estimations

Objects with embedded YSOs will emit strongly not only in the wavelengths ≥70 μm, but also in the mid- and near-infrared. To obtain a realistic estimate of the bolometric luminosity, we integrated the fluxes between 3 μm and 1.3 mm, using our obtained flux measurements complemented with, when available, the mid-infrared (3.4–22 μm) fluxes from the *WISE* catalogue (Wright et al. 2010). All data points used to obtain the bolometric luminosity are plotted in Fig. 4 and the resulting luminosity $L_{\rm bol}$ is given in Table 2.

For clump H-1, which contains the UC H II region, we estimated the stellar type based on the bolometric luminosity, under the assumption that the luminosity is dominated by the most massive object, using the zero-age main-sequence (ZAMS) column of table 1 of Panagia (1973). With respect to the previous, lower resolution *IRAS* observations (Wood & Churchwell 1989), we find a lower bolometric luminosity and a slightly later spectral type (O7.5 with respect to the previous O6) due to a lower level of confusion. Using the more recent O star parameters of Martins, Schaerer & Hillier (2005), the spectral type becomes O8. Our spectral type result, O7.5 or O8, reconciles the infrared-based spectral type with the one determined from radio properties – O7.5 (Wood & Churchwell 1989) and O8 (Roshi et al. 2005).

Bolometric luminosities and envelope masses are particularly important quantities, because they allow us to assign an age estimation to the object that is forming in the clump or core following the evolutionary tracks from Saraceno et al. (1996) for low-mass stars and Molinari et al. (2008) for high-mass stars. In the L/M diagram, stellar evolution is represented in two main phases: the stellar accretion phase and the envelope clean-up phase. The first phase is when the forming star is accreting matter from the envelope, which increases its luminosity. Mass accretion stops when the star begins to burn hydrogen burning, i.e. when it arrives on the ZAMS. During the second phase the protostellar envelope is dispersing, while the luminosity stays roughly constant (within the same order of magnitude).

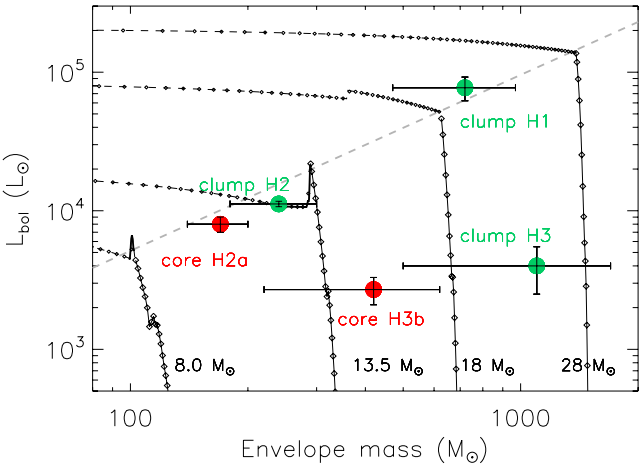

Figure 5. Bolometric luminosity versus envelope mass diagram for the sources in Table 2. Clump H-1, H-2 and H-3 are shown in green, and cores H-2a and H-3b are shown in red. Stellar evolutionary tracks from Molinari et al. (2008) are plotted with the final stellar mass near each track. Open diamonds mark the envelope accretion stage (pre-main-sequence objects): the symbols are in steps of 10^4 yr. Open dots mark the envelope dispersed stage (ZAMS star already formed): symbols are in steps of 10^5 yr. The dashed grey line shows the log–log fit to the IR-primary sources (objects that could be fitted with an embedded ZAMS model and that had the most massive envelope) from Molinari et al. (2008) representing the ZAMS line.

The stellar evolution tracks in the L/M diagram assume the formation of single objects. A rough idea of the impact of multiplicity can be made invoking the Salpeter's initial mass function:

$$N = k_1 M^{-1.35}, \quad (2)$$

where N is the number of objects and M is the stellar mass. It shows that most of the mass is in lower mass objects. When the luminosity is determined by the stellar luminosity, it can be related to the mass by $L \propto M^{3.5}$ and it will be dominated by the more massive objects. Hence, the envelope mass will be much more affected by the multiplicity than the luminosity.

Fig. 5 shows the location of clumps H-1, H-2, H-3, and cores H-2a and H-3b on the L/M diagram. We estimated the age range from the two stellar tracks that surround the clump or core, for example for clump H-1 we used the 18 and 28 $M_\odot$ stellar tracks. The obtained age ranges and average ages are listed in Table 2. The difference between using the masses and luminosities of cores rather than the clumps is that cores are less massive and slightly less luminous. This puts the cores on less massive evolutionary tracks which are evolving slower, and hence the ages become larger. Since the L/M diagram assumes the objects to be single, the core ages should be more accurate than those of the clumps and in the rest of the paper we will use the ages of cores H-2a and H-3b, rather than those of clumps H-2 and H-3, For clump H-3 to core H-3b, the evolutionary stage did not change very much: both objects are in the envelope accretion phase and their ages are similar. The age difference between clump H-2 and core H-2a in the L/M diagram is a little larger due to the more complex behaviour of the stellar tracks in the L/M diagram near the ZAMS line. In the following sections, we present molecular line data to find further relative and absolute age estimates to compare with the L/M-based ages.

Table 3. Derived properties of the CH_3CN cores.

Core	RA ($^h:^m:^s$)	Dec. ($^\circ:':''$)	R (pc)	V_{LSR} (km s^{-1})	Δv_{obs} (km s^{-1})	T_{rot} (K)	N_{CH_3CN} (10^{12}cm^{-2})
H-2a	19:01:45.55	01:13:33.0	0.05	42.7 ± 0.2	1.9 ± 0.4	61 ± 20	8 ± 3
H-3a	19:01:42.65	01:13:37.5	0.06	42.1 ± 0.1	2.2 ± 0.4	44 ± 4	9 ± 6
xx H-3b	19:01:42.31	01:13:33.5	0.08	42.0 ± 0.2	2.3 ± 0.5	41 ± 6	8 ± 2

Notes. Columns are (from left to right): core name; positions (J2000); radius of CH_3CN core; CH_3CN LSR velocity; CH_3CN line width of $K = 0$ level; CH_3CN rotational temperature; CH_3CN column density.

3.2 Class II methanol masers

We detected the class II 3_1-4_0, A^+ methanol maser transition at 107 GHz towards clump H-2/core H-2a. This is the first interferometric observation of this maser transition in W 48A delivering sub-arcsecond images of the maser spots and their distribution, as previous 107 GHz detections were single dish only (Val'tts et al. 1995). The distribution of 107 GHz methanol maser spots as well as their correlation with the 6.7 and 12.2 GHz methanol masers (Minier et al. 2000) is discussed in Appendix B. The class II methanol maser detection towards clump H-2 is important, as class II methanol masers are thought to be exclusively associated with high-mass star formation (Menten 1991; Minier et al. 2003), which, despite some recent doubts, has been confirmed again (Breen et al. 2013). Class II methanol masers are excited before and during the onset of the H II region, and hence to have younger or similar ages, i.e. $\lesssim 10^5$ yr (Walsh et al. 1998; Codella & Moscadelli 2000; Breen et al. 2010).

3.3 Methyl cyanide (CH_3CN) emission

CH_3CN is a commonly observed molecule in hot molecular cores, which are regions of high-density molecular gas surrounding an intermediate- to high-mass YSO. The YSO elevates the dust temperatures (>100 K) in these regions, which causes the evaporation of the icy grain mantles and the increase of the CH_3CN gas phase abundance by several orders of magnitude (Olmi, Cesaroni, Neri & Walmsley 1996; van der Tak, van Dishoeck & Caselli 2000; Purcell et al. 2006). The CH_3CN observations had a high angular resolution (see Table 1) allowing us to observe core-sized (<0.1 pc radius) objects and to find the first signs of fragmentation in the clumps detected with *Herschel*. The integrated intensity CH_3CN map in Fig. 3 shows that CH_3CN is concentrated towards three cores, whose continuum properties are described in Section 3.1.1. The most compact core H-2a, which appears to be unresolved, overlaps with clump H-2, while clump H-3 was found to fragment into two CH_3CN cores, H-3a (no continuum emission detected) and H-3b (continuum emission detected). It is probable that the CH_3CN emission at the location of H-3a is extended emission from low-velocity shocks, such as is seen in DR 21 (Csengeri et al. 2011) where it was associated with small-scale convergence flows, rather than the CH_3CN emission associated with a YSO. Such a nature of the CH_3CN emission is plausible, as core H-3a coincides with the red CO(2–1) outflow lobe, which could provide the low-velocity shocks (the outflow is discussed in Section 3.5). No CH_3CN emission was found towards clump H-1.

Spectra integrated over the area of the cores were extracted from the data cube and fitted with GILDAS/CLASS (Pety 2005).[2] The $K = 0$ to $K = 3$ rotational ladder components were detected for all three cores and fitted simultaneously with Gaussian profiles. We constrained the line width of all K levels to be the same, i.e. that of the $K = 0$ component which is given in Table 3. The signal-to-noise ratio for the $K = 4$ component was too low to obtain a reliable fit. The temperature and column density were estimated using the rotational diagram analysis method (see, e.g., Araya et al. 2005) assuming that the regions are optically thin (Turner 1991). In the upper panel of Fig. 6, we show an example of the CH_3CN $K = 0$, 1, 2, 3 component spectrum and its fit. The bottom panel shows the population diagram for the various K levels on which the temperature and column density estimation was based. The positions of the cores and results of the fits are given in Table 3.

The optical depth can be calculated once the rotational temperature is known. If the CH_3CN emission is optically thick, the column densities will be underestimated, while the rotational temperatures will be overestimated (Goldsmith & Langer 1999). We derived optical depths of the order of 0.02. Iterating by the optical depth correction factor ($\tau/(1 - \exp^{-\tau})$), as done by Remijan et al. (2004), we estimated that the corrected column densities and rotation temperatures are the same as those for the optically thin limit within the uncertainties. The calculated CH_3CN column densities of $\sim 8 \times 10^{12}$ cm^{-2} (Table 3) are similar to those found in hot cores (Olmi, Cesaroni & Walmsley 1993; Araya et al. 2005). The rotation temperatures show that core H-2a is warmer than cores H-3a and b, and in addition is also more compact (Table 3). The CH_3CN line thermal widths are all dominated by non-thermal components (thermal CH_3CN line widths for 40–60 K are $\sim$0.2–0.3 km s^{-1}).

3.4 Ammonia (NH_3) emission

The NH_3 (1,1) and (2,2) transitions are excited in dense and cold environments (e.g. Pillai et al. 2006). We analysed the NH_3 data cubes with the GILDAS software fitting the hyperfine structure of the NH_3(1,1) emission and using a Gaussian for the NH_3(2,2) emission. The NH_3 spectra were extracted in the same areas as defined by the continuum clumps and the CH_3CN cores enabling a direct comparison between NH_3, dust and CH_3CN emission. Following Rygl et al. (2010), we then derived NH_3 rotational temperatures and NH_3 column densities of the clumps and cores (see Table 4). As the column densities were calculated based on interferometric observations, we might filter out some of the NH_3 emission; hence, the NH_3 column densities might be higher than the values we found.

Fig. 7 shows the NH_3 spectra of the clumps. Towards clump H-1, we found NH_3 absorption, similar to that towards DR 21 (Cyganowski et al. 2003), indicating that the emission is emanating from cool molecular material in front of the 10^3 K hot UC H II region. The NH_3 rotational temperature of clump H-1, 17.6 K, was much lower than the dust temperature (42 K), which is a possible indication of the NH_3 being more shielded from the UC H II region radiation than the dust. NH_3 emission towards clump H-2 was found

[2] http://www.iram.fr/IRAMFR/GILDAS

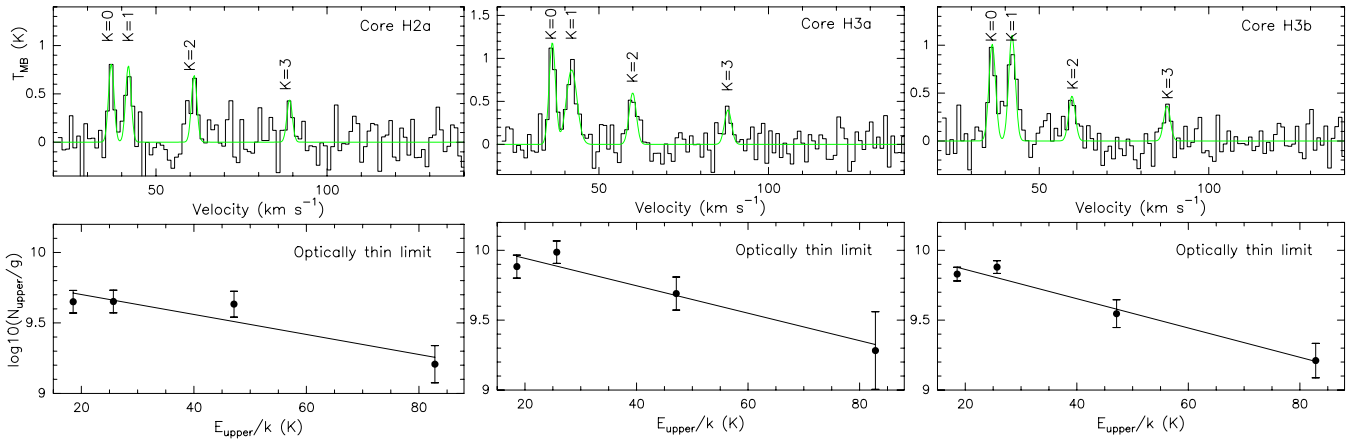

Figure 6. The upper panels show the spectrum of the CH_3CN $K = 0,1,2,3$ transitions and the fit (in green), while the lower panels show the CH_3CN rotational diagram for cores H-2a, H-3a and H-3b. The rest frequency has been set on the $K = 1$ level.

Table 4. Ammonia properties of clumps and cores.

Object	T_{mb}^{11} (K)	Δv^{11} (km s^{-1})	V_{LSR}^{11} (km s^{-1})	τ_m^{11}	T_{mb}^{22} (K)	Δv^{22} (km s^{-1})	V_{LSR}^{22} (km s^{-1})	T_{rot} (K)	N_{NH_3} (10^{15} cm^{-2})
Clump H-1	-0.22 ± 0.10	1.87 ± 0.18	42.92 ± 0.08	1.74 ± 0.67	-0.11 ± 0.02	2.18 ± 0.37	43.04 ± 0.17	18 ± 7	3.9 ± 2.2
Clump H-2$_1$	0.19 ± 0.08	1.34 ± 0.16	42.99 ± 0.08	1.30 ± 0.5^a	0.18 ± 0.03	2.00 ± 0.26	42.84 ± 0.11	40 ± 41	–
Clump H-2$_2$	0.22 ± 0.09	1.26 ± 0.13	45.60 ± 0.06	1.3 ± 0.50^a	0.14 ± 0.03	1.74 ± 0.30	45.47 ± 0.13	24 ± 13	–
Clump H-3	0.65 ± 0.07	1.84 ± 0.06	42.23 ± 0.02	2.47 ± 0.24	0.47 ± 0.03	2.26 ± 0.10	42.17 ± 0.04	22 ± 3	6.3 ± 1.1
Core H-2a$_1$	1.17 ± 9.57	1.49 ± 0.28	42.87 ± 0.10	0.22 ± 1.80	0.24 ± 0.05	1.73 ± 0.27	42.78 ± 0.10	–	–
Core H-2a$_2$	–	–	–	–	0.10 ± 0.05	1.59 ± 0.63	45.26 ± 0.29	–	–
Core H-3a	0.72 ± 0.08	1.68 ± 0.05	42.17 ± 0.02	2.47 ± 0.22	0.52 ± 0.03	2.13 ± 0.10	42.13 ± 0.04	22 ± 3.2	6 ± 1.0
Core H-3b	0.75 ± 0.09	1.79 ± 0.06	42.18 ± 0.03	2.81 ± 0.28	0.58 ± 0.04	2.25 ± 0.11	42.15 ± 0.04	23 ± 3.9	7 ± 1.4

Notes. Columns are (from left to right): name of object; NH_3 (1,1) main beam brightness temperature; NH_3 (1,1) line width; NH_3 (1,1) LSR velocity; NH_3 (1,1) main group opacity; NH_3 (2,2) main beam brightness temperature; NH_3 (2,2) line width; NH_3 (2,2) LSR velocity; NH_3 rotational temperature; NH_3 column density.

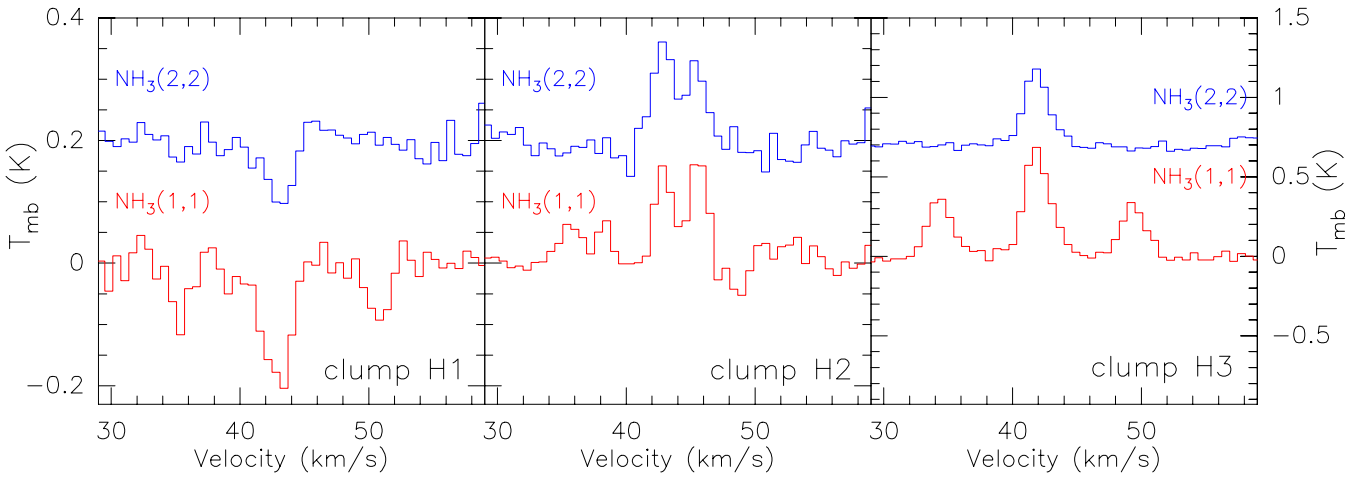

Figure 7. NH_3 (1,1) and (2,2) spectra of clumps H-1, H-2 and H-3. The left-side *y*-axis gives the main beam temperature scale for the clump H-1 and H-2 spectra, while the right-side *y*-axis gives the main beam temperature scale for the clump H-3 spectra. The NH_3 (2,2) spectra have been offset artificially.

to have two components (around 43 and 45.6 km s^{-1}), making the fitting of the lines more difficult. We fixed the optical depth (and its error) at 1.2 ± 0.5 for both components when performing the line fit. The two velocity components are also found in the $C^{18}O$ spectra (see Section 4.2.1), where the 43 km s^{-1} component is correlated with the ridge emission and the 45 km s^{-1} component is thought to emanate from the arc-like structure around the UC H II region. Unfortunately, the temperature estimations have too large uncertainties to provide more detailed information on these two velocity components.

Clump H-3 had the strongest NH_3 emission among the three clumps. Its NH_3 rotational temperature (22 K) was found to be in very good agreement with the dust temperature (20 K). The NH_3

properties of clump H-3, which overlaps with Pillai et al. (2011) NH_3 core no. 3, are in agreement with the rotational temperatures and NH_3 column densities derived by those authors. The CH_3CN rotational temperatures were higher than the NH_3 temperatures, which is expected since CH_3CN traces warm regions near the YSO, while NH_3(1,1) and (2,2) trace colder gas. The NH_3 analysis of core H-2a yielded similar numbers as for clump H-2, except that for the NH_3 (1,1) line we did not detect the 45.6 km s^{-1} component due a higher noise in the core spectrum. Similarly, core H-3a and b have similar NH_3 properties as clump H-3. The local standard of rest (LSR) velocities of the NH_3 towards the cores H-2a, H-3a and H-3b match well with the CH_3CN velocities, indicating that both molecules trace material with a similar kinematic signature, belonging to the same object.

While the NH_3(1,1) line width is an intrinsic line width (since we fitted the hyperfine structure of the transition), the NH_3(2,2) width is not: it is an overestimate of the intrinsic line width. For both NH_3 and CH_3CN, the line widths are dominated by the non-thermal line width, since thermal line widths for NH_3 are of the order of 0.2–0.3 km s^{-1} for temperatures of 20–30 K. For all cores, the NH_3 (1,1) and (2,2) line widths were both much broader than those of CH_3CN ($\sim$1–1.2 km s^{-1}). Possibly, the CH_3CN emission emanates from a smaller area near the YSO, while the NH_3 emission comes from a larger volume containing more turbulence in the surrounding medium by possible discs and outflows (see the outflow in clump H-3 in Section 3.5).

3.5 Outflows

Molecular outflows are commonly observed in low-mass and high-mass star-forming regions (see, e.g., Phillips et al. 1988; Beuther et al. 2002; López-Sepulcre et al. 2009; Duarte-Cabral et al. 2013; Rygl et al. 2013). Outflows arise from the mass accretion on to the molecular clump (e.g. Shepherd & Churchwell 1996), and are often accompanied by maser emission due to the shocks created by the outflow [e.g. see the water masers in the outflow of W3(OH) in Hachisuka et al. (2006)]. Molecular outflows can be observed through optically thick emission of common interstellar medium constituents, such as ^{12}CO.

The HARP CO (3–2) data revealed an outflow in clump H-3. In Fig. 8, we show the integrated emission of the high-velocity wings. The blue and red high-velocity lobes are quite compact indicating that the outflowing material is collimated and that clump H-3 must be hosting active star formation activity. A comparison with 70 μm emission, tracing mainly warm dust near YSOs, shows that core H-3b (rather CH_3CN core H-3a) is the more likely origin for the outflow since it coincides with the 70 μm source. The CO (3–2) outflow lobes coincide with the lower resolution HCO^+(1–0) outflow lobes discussed by Pillai et al. (2011) (see Fig. 8). The displacement between the CO outflow lobes and the *Herschel* dust continuum is real, since it is greater than the sum of the position uncertainties of the JCMT CO data (2 arcsec) and BIMA CH_3CN data (0.4 arcsec). Also the HCO^+(1–0) outflow and the 3 mm continuum emission in Pillai et al. (2011) show the same displacement. Apparently, the outflow axis is not straight, which is why the blue and red lobes are not symmetrical around the continuum source. Pillai et al. (2011) estimated the outflow mass to be about 5 $M_\odot$, indicating that core H-3b is driving a massive outflow. In addition to this massive molecular outflow, clump H-3 also hosts water masers (Hofner & Churchwell 1996) located towards the red outflow lobe. The detection of the massive outflow and water masers indicates that clump H-3 is in an active star formation stage, hence presumably younger than the other two clumps H-1 and H-2, which do not exhibit any collimated outflows.

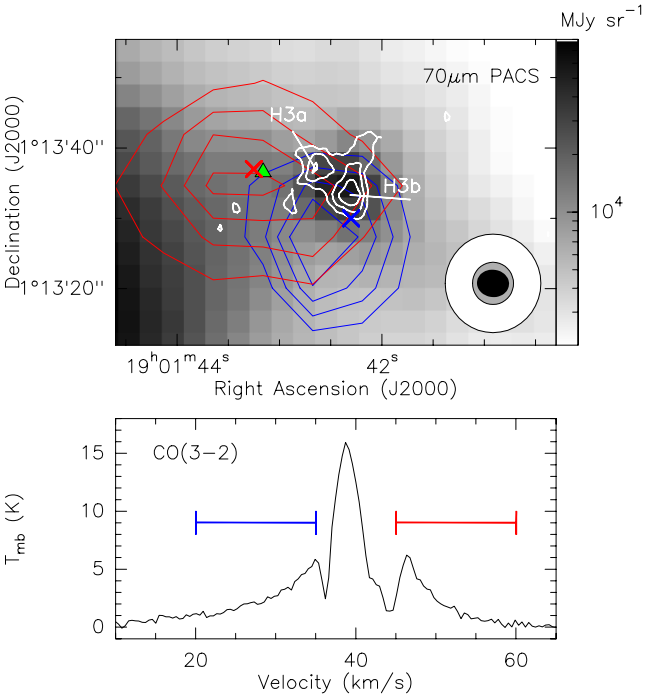

Figure 8. Top panel: 70 μm PACS grey-scale map centred on clump H-3 with the JCMT CO (3–2) outflow (blue, red) and the CH_3CN cores (white) overlaid in contours. CO contour levels are 20, 30, 40 and 50 K km s^{-1} for both blueshifted and redshifted material. BIMA CH_3CN contour levels are 0.06, 0.08, 0.10 and 0.12 Jy beam^{-1} km s^{-1}. Beam sizes of the CO (3–2) (white), PACS 70 μm (grey) and CH_3CN emission (black) are given in bottom-right corner. The green triangle represents the water maser location (Hofner & Churchwell 1996), the blue and red crosses mark the HCO^+ outflow lobes from Pillai et al. (2011). Bottom panel: the CO(3–2) spectrum towards clump H-3 where the velocity ranges used for mapping of the blueshifted and redshifted outflow lobes are indicated.

4 RESULTS AND ANALYSIS OF EXTENDED EMISSION

4.1 *Herschel* continuum emission

We computed column density and temperature maps from the calibrated 160–500 μm images, after these were convolved to the 500 μm resolution (36 arcsec) and rebinned to the pixel size of the 500 μm map (11.5 arcsec). Then, pixel-by-pixel modified blackbody fits were performed on the regridded maps (see Elia et al. 2013 for the expression and its details). We assumed a dust opacity κ_ν of $\kappa_\nu = \kappa_0(\frac{\nu}{\nu_0})^\beta$ with $\kappa_0 = 0.1$ cm^2 g^{-1} (which includes a gas-to-dust ratio of 100) and $\nu_0 = 1200$ GHz (250 μm) (Hildebrand 1983). The dust emissivity index β was kept constant at 2.0. Recent studies (e.g. Juvela et al. 2011; Miettinen et al. 2012; Sadavoy et al. 2013) show that β varies across the cloud. While some works point out the anticorrelation between the dust temperature and β, Bayesian SED fitting finds an anticorrelation of β with column density rather than temperature (Kelly et al. 2012). Ysard et al. (2013) find that the change in β is due to dust properties and varies with density. Our *Herschel*-only data (the SCUBA, MAMBO and BIMA dust continuum maps had a much smaller coverage, so were not used for the large-scale temperature and column density maps) are not able

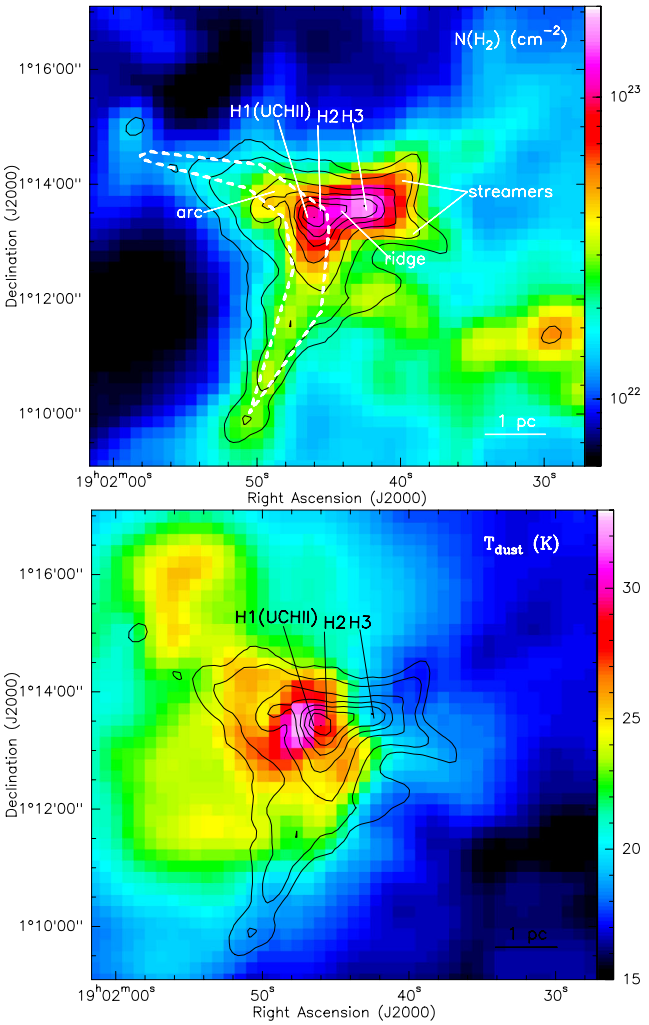

Figure 9. *Herschel* H_2 column density and dust temperature maps of the W 48A surroundings. Clumps H-1, H-2 and H-3 are marked, just as the large-scale structures: the arc (white dash), the ridge and the streamers. Contours show the SPIRE 250 μm emission between 2000 and 55 000 MJy sr^{-1} using a square root scaling.

to constrain the β. Using $\beta = 2.0$ with χ^2 fitting (as we do) can cause the resulting temperature to be too low in the case $\beta < 2.0$ and vice versa, as shown by Sadavoy et al. (2013). Furthermore, to obtain the H_2 column density, we used the mean molecular weight per hydrogen atom $\mu_H = 2.8$ (Kauffmann et al. 2008). Recent HOBYS studies, such as e.g. Hill et al. (2012), often use a mean molecular weight of 2.3 which is averaged per particle instead per hydrogen atom and results in higher column densities by a fixed factor of 2.8/2.3 ∼ 1.2.

Fig. 9 displays the resulting temperature and column density maps of W 48A with the 250 μm contours overplotted. As expected, the 250 μm contours match very well with the column density map, but are quite different from the temperature map, which traces the warm dust heated by YSOs and stars. The column density map shows a north-west oriented arc around the UC H II region (dashed contours, Fig. 9) directed towards a dense ridge[3] running east–west from clump H-1 till clump H-3, and diverging into two 'cold streamers', westwards of clump H-3. The morphology of the arc suggests that it was shaped by the UC H II region. The temperature map (Fig. 9) shows how the W 48A UC H II region is heating up the surroundings. Heating of dust by (young) stars has been seen in many *Herschel* observations (see, e.g., Zavagno et al. 2010a; Hill et al. 2012; Minier et al. 2013). Towards the low-density region, south-east of the UC H II region, there is a bubble of heated dust (≥25 K) with respect to the background temperature (∼16 K), while towards the more dense material the heating is less efficient: the ridge ($T \leq 26$ K) and especially the streamers ($T \leq 20$ K) are composed of colder dust than the UC H II region (∼28 K). With a molecule like NH_3 we can use the ratio of the (2,2) to (1,1) main beam temperatures (T_{22}/T_{11}) to find heated molecular gas (Torrelles et al. 1989; Zhang et al. 2002). The VLA NH_3 data find the highest T_{22}/T_{11} near core H-2 (see Fig. C1), suggesting that it might be heated by the UC H II region, and consistent with the presence of a PDR as seen near other UC H II regions (e.g. Palau et al. 2007).

The cold streamers seen by *Herschel* were first noted by Pillai et al. (2011), who found several NH_2D cores just westwards of clump H-3 using interferometric PdBI data. To deuterate NH_3, creating the NH_2D molecule, very cold temperatures ($T < 15$ K; Bergin & Tafalla 2007) are required. Protostellar heating of the environment, which would increase the temperature $T > 20$ K, would destroy the NH_2D. Therefore, the detection of NH_2D cores indicates that in this region no protostars have been formed yet. These NH_2D cores were not detected in the *Herschel* maps, nor in the high-resolution 1.3 mm PdBI data of Pillai et al. (2011), showing that at small core-like scales the deuterated gas differs from the dust distribution, while on larger scales (as 1 pc, such as the streamers) the correlation between the dust and NH_2D emission is remarkably good. The *Herschel* dust temperature and column density map shows that these streamers have indeed the lowest dust temperature of the whole W 48A environment and that they are dense structures. We conclude that the cold streamers represent the earliest star formation stage observed in the W 48A star-forming region.

4.2 Kinematics

4.2.1 $C^{18}O$ (1–0) gas kinematics near the UC H II region

We proceed with the exploration of the kinematics of the extended structures of the W 48A star-forming region through the $C^{18}O$ (1–0) data. The BIMA+IRAM30 m $C^{18}O$ (1–0) integrated intensity map (Fig. 10, left-hand panel) shows a large area of emission around the head of the arc and a horizontal extension (the ridge) with several bends, which ends near the H-3 clump. The peak of the $C^{18}O$ (1–0) emission is near the H II region. To investigate the gas kinematics, we made a $C^{18}O$ position–velocity plot (right-hand panel of Fig. 10) to show the $C^{18}O$ (1–0) intensities at each velocity bin along the cut across the arc and the ridge (indicated in the left-hand panel). The ridge has a quite simple velocity structure: a very narrow velocity range ($42 < V_{LSR} < 43$ km s^{-1}) including the CH_3CN LSR velocities along the ridge and is considered to be 'at rest'. Near the UC H II region, the kinematics become more interesting. There is a receding arc at angular offsets <40 arcsec, velocities 42–45 km s^{-1} and some material in front of the UC H II region (at 40 arcsec). Together they might create a shell structure that is similar to the expanding bubbles in the model of Arce et al. (2011). However, unlike in Arce et al. (2011) our source is not a bubble, but an arc or a shell. Also there is more material redshifted than blueshifted, indicating that we are not dealing with a symmetrical structure, and making the word 'arc' more appropriate than 'shell'. Fig. 10 suggests that the UC

[3] The word ridge is used to indicate an filamentary cloud with a column density >10^{23} cm^{-2} (see Hill et al. 2011).

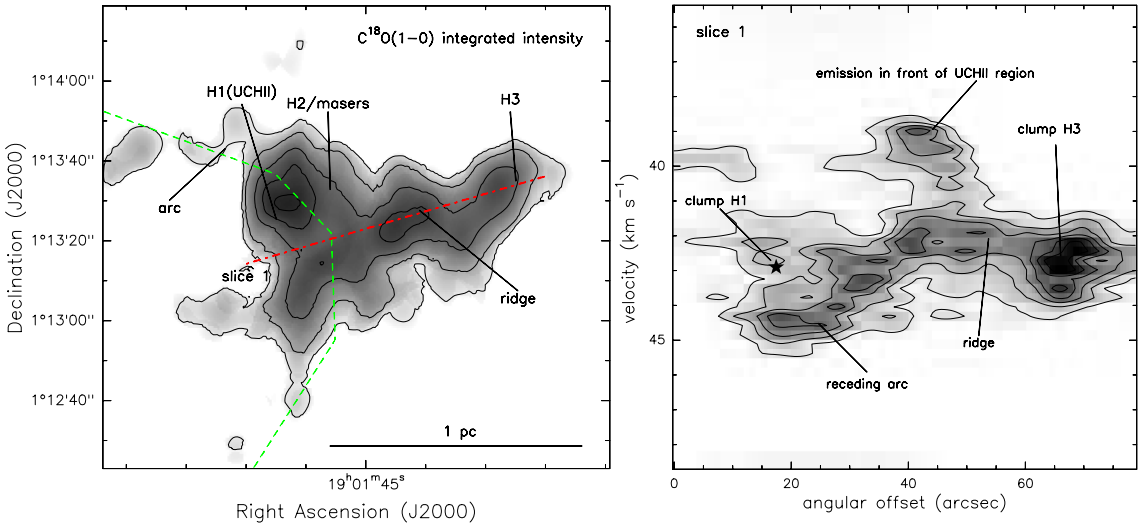

Figure 10. Left-hand panel: BIMA+IRAM 30 m integrated intensity map of the $C^{18}O$ emission. Clump H-1 (W 48A UC H II region), core H-2a (maser source and clump H-2), clump H-3, the ridge and the arc are marked. Contours are 0.25, 0.5, 1.0, 1.5 and 2.0 Jy beam^{-1} km s^{-1}. Right-hand panel: position velocity plot along the red dash–dotted line in the left figure. Contours are 0.15, 0.25, 0.35, 0.45, 0.55, 0.65 and 0.75 mJy beam^{-1}. The various velocity components are marked on the plot.

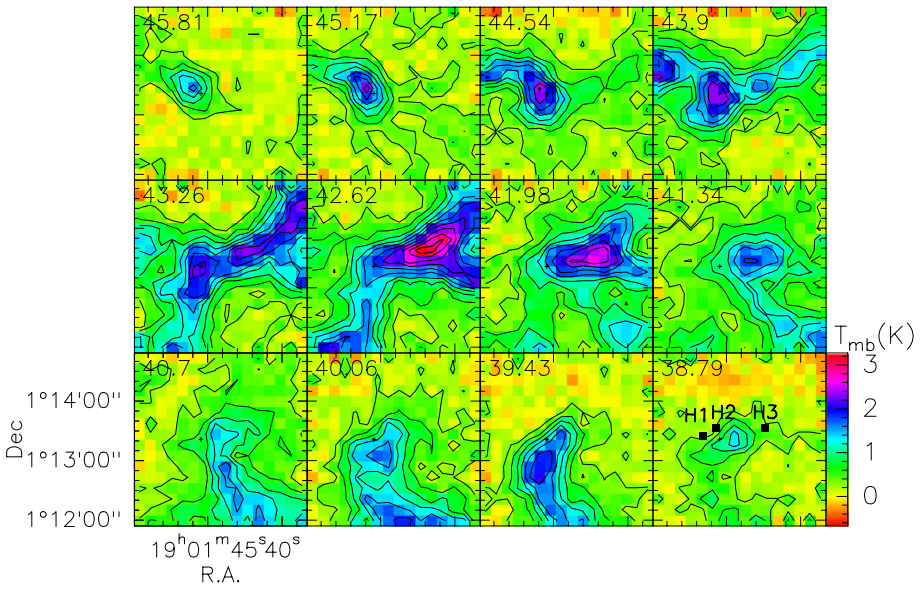

Figure 11. IRAM 30 m $C^{18}O$ (1–0) channel map smoothed to a channel spacing of 0.64 km s^{-1} for a better visualization. Central velocity of each channel is marked in the top-left corner. The map noise is 0.13 K and the contour spacing is 0.3 K (2.3σ). Black squares indicate clumps H-1, H-2 and H-3.

H II region formed on the near side of the ridge, and during its evolution pushed most of the dense gas away to be redshifted. A smaller amount of material surrounding the UC H II region ended up blueshifted or at rest.

To visualize the multiple velocity components, we use the IRAM 30 m $C^{18}O$ (1–0) channel map (Fig. 11) as the single-dish $C^{18}O$ data covered a larger area (the $C^{18}O$ BIMA data were limited by the field of view). The $C^{18}O$ emission seems to be a mixture of three main velocity components, one around 38–41 km s^{-1} (which we name the 'blue' component, see bottom four panels in Fig. 11), one around 41–43.5 km s^{-1} (the 'green' component, the middle four panels in Fig. 11) and one around 44–45 km s^{-1} (the 'red' component, top four panels in Fig. 11). The arc is clearly visible: starting south-east of clump H-1 (UC H II region) at $V_{LSR} = 42.6$ km s^{-1} and proceeding northwards towards clump H-1 and from there north–eastwards at $V_{LSR} = 44.5$ km s^{-1}, covering a velocity gradient of $\sim$2 km s^{-1}. The green velocity component contains most of the $C^{18}O$ emission: it correlates well with the dust continuum and the column density map: the ridge, the streamers and the middle-southern part of the arc are all visible. This not surprising since this velocity range also includes the LSR velocities of the clumps and cores. What looked one arc in the dust continuum seems to kinetically be more

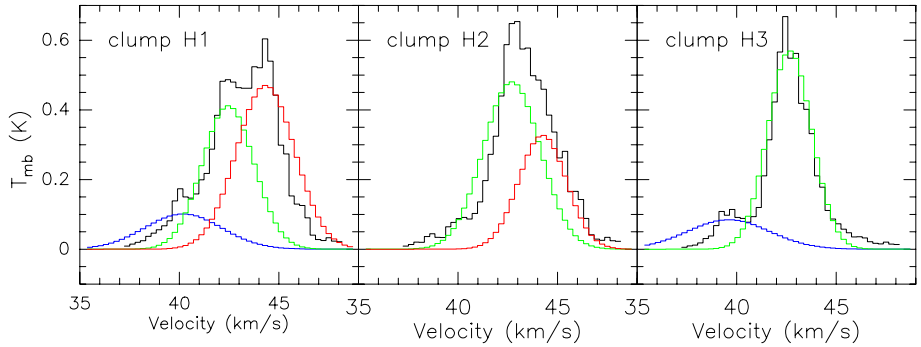

Figure 12. BIMA+IRAM 30 m $C^{18}O$ (1–0) spectra towards clumps H-1, H-2 and H-3, showing the Gaussian fits of the three velocity components in different colours.

complicated: the middle-northern part of the arc is receding, and the southern part of the arc is at rest or advancing. This points either to two uncorrelated velocity structures or to an arc which is inclined to result in the observed perspective. We obtained the clump $C^{18}O$ spectra from the high dynamic range BIMA+IRAM 30 m data and fitted a Gaussian to each velocity component (Fig. 12). The green velocity component is found towards all three clumps, while the red component is found only towards H-1 and H-2. The blue component, seen towards clumps H-1 and H-3, is always much weaker than the green or the red component.

4.2.2 $^{13}CO(1–0)$ emission tracing material in front of the UC H II region

This blue $C^{18}O$ velocity component, introduced in the previous section, is different from the red and green $C^{18}O$ components. Namely, while the red and green $C^{18}O$ have a similar distribution to the dust emission, the blue $C^{18}O$ does not. When one compares the V_{LSR} = 38.79 km s^{-1} channel map in Fig. 11 with the column density map in Fig. 9, one can notice that none of the high-density structures are coinciding with the blue $C^{18}O$ emission. In fact, the blue velocity component correlates well with the *Ks*-band absorption features, which are caused by material in front of the UC H II region (Fig. 13).

Our BIMA data set included ^{13}CO observations. As ^{13}CO is about 10 times more abundant in cold molecular clouds than $C^{18}O$ (see e.g. Du & Yang 2008 and references therein), it is often observed to be optically thick, even where $C^{18}O$ is still optically thin. Therefore, it can be used to visualize the location of low-density molecular gas. If there was optically thick molecular gas in front of the UC H II region, the ^{13}CO emission would have the same shape as the near-infrared absorption, as we indeed see in Fig. 13. The correlation of the blue $C^{18}O$ component, the *Ks* absorption and the ^{13}CO emission suggests that it traces low-density material in front of the UC H II region.

5 DISCUSSION

5.1 W 48A revisited

Roshi et al. (2005) sketched the W 48A UC H II region as a PDR-dominated H II region, where the ionizing star is moving with respect to the molecular cloud. Their C76α radio recombination line (RRL) measurements showed that the PDR (V_{LSR} = 41.9 km s^{-1}) was moving at 2.5 ± 1 km s^{-1} into the molecular cloud for which they took V_{LSR} = 44 km s^{-1} (Churchwell, Walmsley & Wood 1992). The

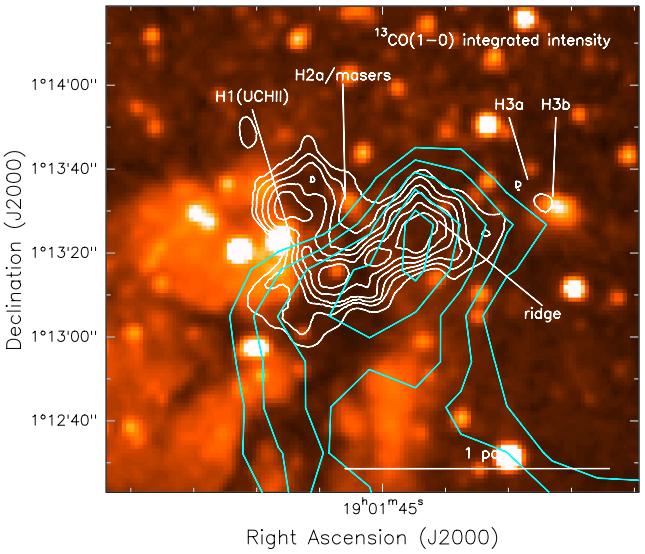

Figure 13. 2MASS *Ks*-band (2.16 μm) image overlaid with ^{13}CO integrated intensity contours (white) and the blue $C^{18}O$ velocity component (38–41 km s^{-1}, cyan).

LSR velocities of our $C^{18}O$ (1–0) data show that the molecular cloud covers a range of velocities from ∼41 up to 45 km s^{-1}. The LSR velocity of the C76α line falls in the velocity range of the molecular material: the PDR is moving *at the same velocity* as that part of the cloud.

To understand if the PDR is pressure confined by the molecular material, we use the formulae given in Roshi et al. (2005) and calculate the pressure of the molecular cloud. The molecular cloud pressure is given by the sum of the pressure from thermal processes and from turbulence (Xie et al. 1996). Roshi et al. (2005) demonstrated that this $P_{PDR} = 5.3–43.0 \times 10^{-7}$ dyne cm^{-2} > $P_{UC\,H\,II}$ = 1.3×10^{-7} dyne cm^{-2} and that therefore the UC H II region is pressure confined by the PDR. Now, the pressure in the molecular material in the ridge is given by

$$P_{mol} = n_{H_2} \left(k_B T_{mol} + \mu m_H d v_{mol}^2\right), \quad (3)$$

where T_{mol} = 26 K (from the dust temperature map), μ = 2.8 and dv_{mol} =1.0–1.8 km s^{-1} based on $C^{18}O$ (1–0) and NH_3 (1,1) line widths resulting in $P_{mol} = n_{H_2} 1 \times 10^{-13}$ dyne cm^{-2}. Using the NH_3 rotational temperature (22 K) would yield a similar outcome. Estimates of the volume density based on the column density map

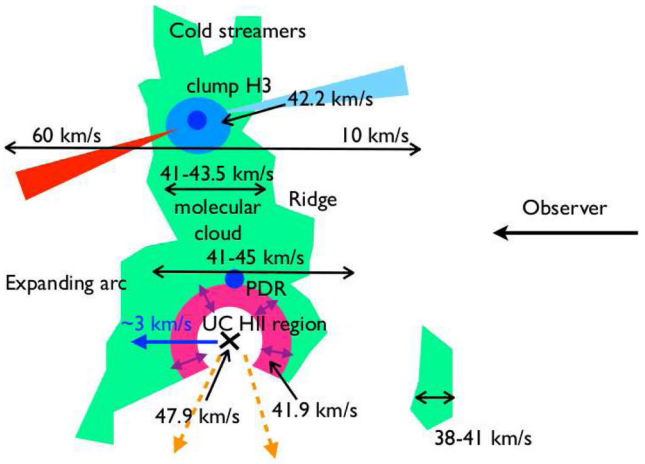

Figure 14. Schematic drawing of the W 48A star-forming region. The cross marks the location of the UC H II region (white) with an LSR velocity of 47.9 km s^{-1} (Wood & Churchwell 1989). The PDR is pink and has an LSR velocity of 41.9 km s^{-1} (Roshi et al. 2005). The molecular cloud is green and contains a wider range of velocities. The purple arrows in the PDR show that it is expanding. Core H-2a is marked in dark blue at the border of the PDR. Light blue marks clump H-3 with the H-3b core inside it in dark blue. The molecular outflow of clump H-3 is shown by a red and blue cone indicating also the velocity range. The UC H II region is moving away with about 3 km s^{-1}. The champagne flow of the UC H II region is indicated by dashed yellow arrows.

depend on the depth of the ridge. Assuming the same depth as width (∼1 pc), the volume density of the molecular material in the ridge would be 6×10^4 cm^{-3}. This would bring the pressure of the molecular material to 6×10^{-9} dyne cm^{-2}, much lower than the PDR pressure. To stop the PDR from expanding into the molecular cloud, $P_{\rm mol}$ would have to be larger than $P_{\rm PDR}$ which would require molecular hydrogen densities of 10^8 cm^{-3}. However, our hydrogen density estimate for the ridge is several orders of magnitude smaller. Therefore, the PDR is expanding into the cloud and pushing the molecular material outwards, maintaining the arc-like structure. To fully appreciate the role of the PDR, high-sensitivity RRL imaging of the W 48A UC H II region and its surroundings would be necessary to trace the PDR kinematics. Finally, Roshi et al. (2005) found that the UC H II region is receding with a few (∼3) km s^{-1}, which might explain why the arc is receding rather than advancing with respect to the LSR velocity of the ridge. In Fig. 14, we modify the view of Roshi et al. (2005) to reflect the results of our observations.

5.2 Comparison of age estimates

In Section 3.1.1, we derived the ages of the clumps/cores based on the L/M tracks of Molinari et al. (2008) to be $\sim 8 \times 10^5$ yr for clump H-1 (UC H II region) and core H-2b (maser core), and $\sim 1.5 \times 10^5$ yr for core H-3b (containing the molecular outflow). These ages contain many uncertainties: the uncertainties of the envelope masses and bolometric luminosities, and those from stellar evolution models used for the stellar tracks. It is therefore useful to compare these age estimations with the results from radio continuum data, molecular line data and the literature.

Radio continuum and RRL measurements (Wood & Churchwell 1989; Onello et al. 1994; Roshi et al. 2005) unmistakably showed that the object matching with clump H-1 is a UC H II region. Literature ages of UC H II regions are similar to our age estimate: 6×10^5 yr (Motte et al. 2007) and $\sim 10^5$ yr (Wood & Churchwell 1989; Akeson & Carlstrom 1996).

Apart from water and hydroxyl masers, core H-2a contains several class II methanol maser transitions, indicating the presence of a high-mass star in formation (Breen et al. 2013). Methanol masers are thought to be excited before the onset of the H II region and be quenched by the ionizing radiation of the star (during the H II region phase), and should hence have younger or similar ages as H II regions, i.e. $\lesssim 10^5$ yr (Walsh et al. 1998; Codella & Moscadelli 2000; Breen et al. 2010). The detection of CH_3CN, a molecule typical of intermediate- to high-mass protostellar objects such as hot cores (e.g., Olmi et al. 1996; Araya et al. 2005; Purcell et al. 2006), and the absence of a compact radio source (due to the free–free emission of the ionizing star, which is typical of H II regions) also agree with a younger evolutionary stage than a UC H II region or a deeply embedded UC H II region. Higher sensitivity radio observations could test if the object might possibly be a hyper-compact H II region.

Core H-3b was found to contain a high-mass YSO identified by the massive collimated outflow observed in CO (3–2) emission (Section 3.5) and the HCO^+(1–0) line (Pillai et al. 2011). We detected NH_3 and CH_3CN emission and obtained the [CH_3CN]/[NH_3] abundance ratio, which can be used as a chemical clock (Charnley, Tielens & Millar 1992). The abundance ratio found towards core H-3b was $\sim 1 \times 10^{-3}$ (see Tables 3 and 4), which is similar to the typical hot core abundance ratio of [CH_3CN]/[NH_3] $\sim 10^{-3}$ that corresponds to ages of $\sim 6 \times 10^4$ yr (Charnley et al. 1992). Literature ages for hot cores (high-mass protostellar objects) are between 2×10^4 yr (Motte et al. 2007) and 5×10^4 yr (Cazaux et al. 2003). These two age estimates are both lower than what we obtained from the L/M diagram.

Using several molecular lines and radio continuum data, we could infer that (1) clump H-1 is indeed the most evolved and oldest object, (2) core H-2a is in an earlier evolutionary stage than clump H-1 and most likely also younger than clump H-1, while the L/M diagram-based age estimation found similar ages for these two objects, and (3) that core H-3b is indeed the youngest and less evolved object. Given that all three objects are forming high-mass stars, the evolutionary difference is likely to reflect the age difference, since high-mass stars evolve along similar tracks, i.e. change their envelope mass and luminosity on similar time-scales. It is thus important to have higher resolution submm or radio continuum data and molecular line data to complement the age estimations based on infrared continuum data (such as the L/M diagram).

5.3 Sequential star formation sequence around W 48A?

The top panel in Fig. 15 shows a synthesis of our sequential star formation results in W 48A. In this study, we isolated at least four different stages of star formation and estimated their ages, the UC H II region (clump H-1), the maser core (core H-2a), the active star-forming YSO with outflow (core H-3b) and the cold streamers in which Pillai et al. (2011) found prestellar cores in NH_2D of 50–200 $M_\odot$. The ages of prestellar objects depend strongly on whether they will form low- or high-mass stars. Assuming that these massive prestellar cores will form high-mass stars, then they should have younger ages than hot cores $<5 \times 10^4$ yr (Cazaux et al. 2003). As protostellar heating destroys NH_2D, detecting these prestellar cores indicates that no protostars have been formed yet, which was confirmed through the non-detection of protostellar objects in the 70 μm PACS map. Interestingly, these four stages of star

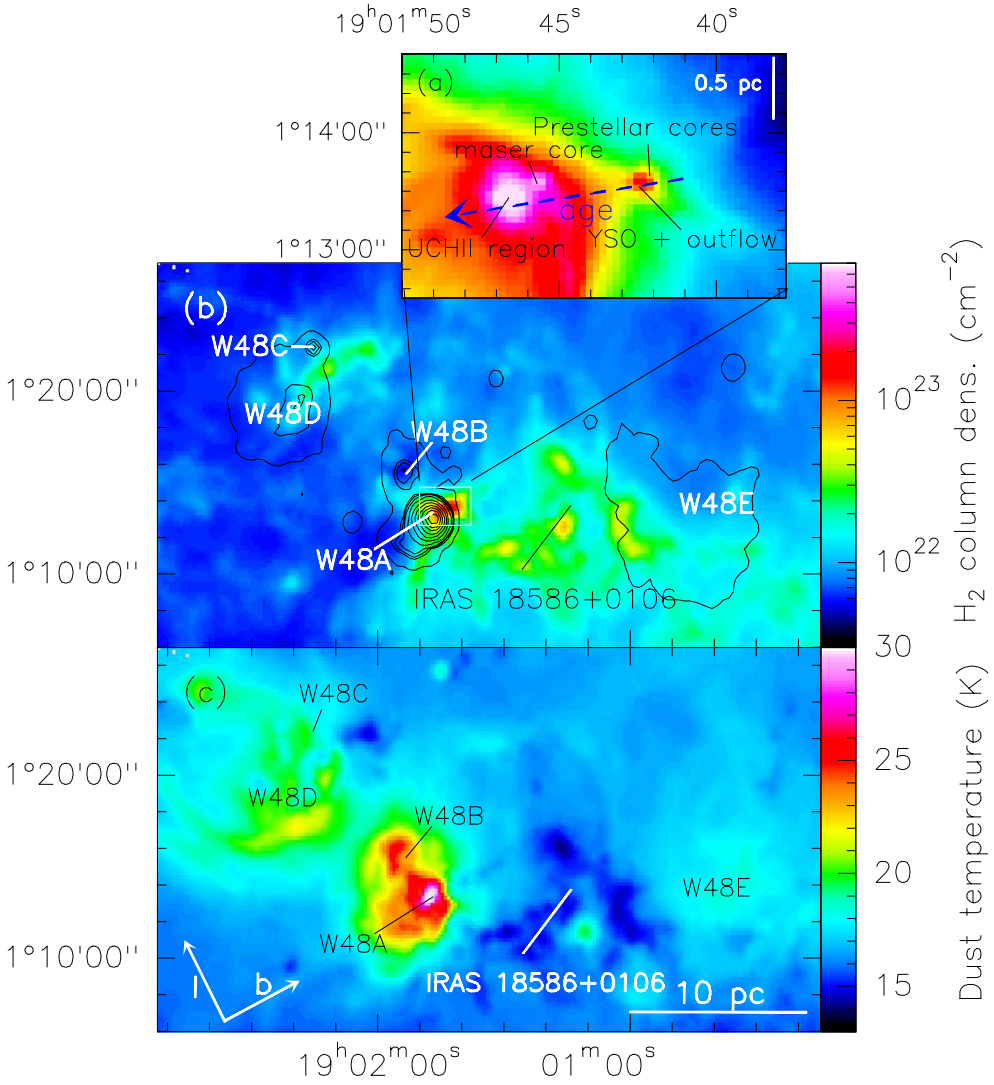

Figure 15. Panel (a): sequential star formation around W 48A indicated on the PACS 70 μm map. Panels (b) and (c): *Herschel* H_2 column density and temperature maps of the W 48 H II region complex (W 48A–E). The column density map is overlaid with the 21 cm contours of the NVSS survey (Condon et al. 1998). The Aquila supershell expansion is oriented in the direction of Galactic latitude, *b*, indicated in the bottom panel.

formation are aligned in an east (old) to west (young) configuration, forming a linear age gradient (Fig. 15, panel a). Large projection effects can, most likely, be disregarded since the objects are forming within the same molecular cloud, suggesting that this remarkable age arrangement is real and reflects the formation history of the W 48 molecular cloud.

Panels (b) and (c) in Fig. 15 show that the UC H II region formed on the border of the molecular cloud. Core H-2a could have either formed before the creation of the arc and was swept up by it or formed in the material collected by the PDR in a collect-and-collapse mechanism (Elmegreen & Lada 1977; Whitworth et al. 1994). It is unlikely that the UC H II region triggered the formation of the W 48A molecular cloud nor the star formation inside it. In the previous section, we mentioned that the UC H II region is confined by the PDR (Roshi et al. 2005), but that the PDR is slowly expanding into the molecular medium. The distance between the UC H II region and clump H-3 is about 1 pc. A shock wave propagating at $\sim$0.3 km s^{-1}, which is the sound speed of the medium at 25 K, would take about 3×10^6 yr. The age of clump H-3 is about an order of magnitude younger than the UC H II region, ruling out the UC H II region (and the PDR) as the triggering agent. Hence, the W 48A molecular cloud and its star-forming seeds were assembled before the onset of the UC H II region in such a way that star formation started in the east and progressed towards the west. The sequential star formation in W 48A reminds of the age gradient seen in the DR 21 molecular cloud which was formed by colliding flows, and has a south (old)–north (young) age gradient (see Csengeri et al. 2011; Hennemann et al. 2012). Given the location of W 48 at almost 100 pc below the Galactic plane, the presence of an age gradient suggests a large-scale external force.

First of all, the location of the other W 48 H II regions cannot explain the age gradient (by e.g. triggering) and it seems more likely that all these H II regions belong to one larger star-forming complex. Based on 21 cm H I line data, Maciejewski et al. (1996) discovered the Aquila supershell, centred at about four degrees below W 48A, at $l = 35°$, $b = -6°$. This shell is expanding from below into the Galactic plane, creating, in addition to a superbubble, a cone-like shape directed at $l = 34.^{\circ}6$, $b = -1.^{\circ}4$, very near

Table 5. 21 cm emission properties of the W 48 H II regions.

H II region	Size (arcsec, arcsec)	Peak flux (Jy beam^{-1})	Int. flux (Jy)	I/P
W 48A	74, 72	4.9	12.8	2.6
W 48B	118, 84	0.12	0.6	5.0
W 48C	50, 49	0.16	0.2	1.3
W 48D	221, 169	0.097	1.8	185.5

Notes. Columns are (from left to right): name; size in major and minor axis at FWHM; peak flux; integrated flux; ratio of integrated to peak flux.

(∼40 arcmin or ∼38 pc) to the W 48 H II regions. The 21 cm H I spectra of the left and centre part of this cone show a clear peak at 40–45 km s^{-1} (fig. 4 of Maciejewski et al. 1996), which overlaps with the LSR velocity of the molecular material of W 48A and of the other H II regions in W 48: 41.2 km s^{-1} for W 48B, 46.7 km s^{-1} for W 48D and 45.5 km s^{-1} for W 48E (Onello et al. 1994). It is therefore likely that the initial molecular cloud in which the W 48 complex of H II regions was formed through the compression of ambient material by the Aquila supershell. Maciejewski et al. (1996) estimated that the total energy of the events creating the Aquila supershell is about $1-5 \times 10^{52}$ erg, corresponding to 10–100 supernova explosions powering the system over 10^7 yr. The W 48 H II regions were formed recently given the supershell's age ($\sim 2 \times 10^7$ yr) and its estimated expansion velocity of about 15 km s^{-1} (which is variable depending on the density of the material it passes through). The distance between the centre of the supershell and the W 48 H II regions is about 4° (230 pc at a distance of 3.27 kpc) and at a velocity of 15 km s^{-1} it would take about 1.5×10^6 yr for the shell to reach the W 48 H II regions, leaving ample time for the W 48 H II regions to evolve into their current state.

At the location of the W 48 H II regions, the supershell's orientation is towards increasing Galactic latitudes. The shell would have therefore first reached the locations of W 48C and D, then W 48A and B, and finally W 48E. Hence, the density structures created by the shell should be older in the eastern side of Fig. 15 and younger in the western side. Most of these H II regions are too evolved to have strong far-infrared emission; hence, it is difficult to estimate their evolutionary stages from their envelope masses and bolometric luminosities. It is more fruitful to look at the size of the ionized hydrogen region (the Strömgren shell) created by the young star, which one can observe through its free–free emission in the centimetre radio continuum. For this purpose, we used the 21 cm maps from the NRAO VLA sky survey (NVSS; Condon et al. 1998). With the AIPS task JMFIT, we fitted 2D Gaussians to the 21 cm emission of W 48A–D obtaining the size, peak flux and integrated flux (Table 5). The ratio of the integrated to peak flux (I/P), listed in the fifth column of Table 5, is a measure of the source compactness (1.0 for a point source and increasing when the source is more extended). W 48D seems indeed to be an old H II region, since its radio emission is very extended and it has possibly triggered another younger and compact H II region, W 48C, which is very compact, hence very young, on one of its borders. The radio emission of W 48B is less extended than W 48D, but more extended than that of W 48A, implying an intermediate evolutionary stage. This is consistent with W 48B already containing a cluster of stars (clearly visible in the near-IR) and being surrounded by a small circular dust arc. Based on the 21 cm radio continuum, we conclude that the H II regions have an evolutionary gradient along Galactic latitude, such as one would expect if these regions were formed by the Aquila supershell. In this discussion, we have neglected W 48E, whose nature, either an H II region or a supernova remnant, is uncertain, since it emits extended weak radio emission and does not contain many YSOs or high dust column densities.

In addition to the W 48 H II regions, IRAS 18586+0106, also known as Mol 87, is located between W 48A and W 48E. IRAS 18586 contains a few massive star-forming clumps (Beltrán et al. 2006), but no centimetre continuum emission, which would indicate free–free emission of young stars, could be associated with them (Molinari et al. 1998), nor methanol or water masers (Fontani, Cesaroni & Furuya 2010). With its NH_3 (1,1) LSR velocity of 38 km s^{-1} (Molinari et al. 1996), IRAS 18586 is very likely to be a part of the W 48 complex. In Appendix D, we analysed the infrared emission of the two clumps found in the *Herschel* maps. Source A, which coincides with the IRAS coordinate centre, is the most evolved source with an age of $\sim 5 \times 10^5$ yr forming an intermediate- to high-mass star. The second source (B) is colder, more massive and younger. For the beginning of star formation in IRAS 18586, we only need to take the estimate of the oldest object into consideration, which is $\sim 5 \times 10^5$ yr. This is younger than most evolved object in W48 A (the UC H II region), and would agree with the predicted age gradient if all these star-forming regions were formed by the cone of the Aquila supershell.

In addition, the *Herschel* column density and temperature maps (Fig. 15) revealed that there exists a large reservoir of dense and cold gas west of W 48A, implying that this region has a high potential to form stars. The morphology of this dense gas suggests that it has not been strongly affected by H II regions or stellar winds, which are known to shape the material into bubbles and shells. East of W 48A, there is much less dense material, and when present it is shaped in shells, bubbles and ridges by H II regions. Hence, the large-scale *Herschel* data support the hypothesis of an east–west evolutionary gradient across the W 48 H II regions, in a roughly similar orientation as the age gradient found around W 48A.

6 SUMMARY

We have presented a combined approach of high-sensitivity *Herschel* continuum observations with high-resolution molecular line data from the BIMA array to study the sequential star formation around the W 48A UC H II region. For the three clumps found with *Herschel*, which include a UC H II region, a maser emitting YSO and a YSO with a massive molecular outflow, we combined age estimations based on envelope mass and luminosity with those from radio continuum, molecular line data and the literature values, and found the ages to agree within an order of magnitude. Confusion of emission and multiplicity affects the L/M-based ages, by moving the star-forming object to more massive stellar tracks and to higher luminosities. We tried to correct for this by rescaling the continuum fluxes of clump H-2 and H-3 to the core-sized objects detected in the BIMA CH_3CN maps. High-resolution continuum observations with ALMA, SMA or CCAT are necessary to reach the fragmentation limit of the cores for obtaining more accurate masses and luminosities. In addition to dust continuum data, radio continuum and molecular line data are crucial to identify the various evolutionary phases and to verify the ages based on envelope masses and luminosities.

The W 48A molecular cloud has a particular shape: it is concentrated along a ridge (the main axis of the cloud) lying in front of an arc (which, from our perspective is oriented towards the cloud)

that partially surrounds the UC H II region. $C^{18}O$ (1–0) line data show that this arc-like structure has two velocity components, the northern part which is receding and the southern part which is at rest/advancing. This arc, or part of it, was most likely created by the UC H II region, when this formed at the eastern edge of the ridge, and is maintained by the overpressured PDR. Based on the age dating of the *Herschel* sources, we found a linear evolutionary gradient across the W 48A star-forming region that we interpreted as an age gradient. This age gradient starts in the east of W 48A with the UC H II region, the oldest object, and traverses the arc following the major axis of the W 48A molecular cloud. Since the UC H II region is pressure confined by the PDR, it could not have formed the W 48A molecular cloud nor triggered the formation of most of the YSOs inside of it.

From the centimetre radio continuum, we found that a similar east (older)–west (younger) orientation, as in W 48A, is also present across the W 48 H II regions. Also, large-scale dust maps show that in the eastern part of W48, the H II regions shaped all the gas and dust around them (more evolved, older), while in the western part we find mostly molecular clouds (less evolved, younger). We therefore considered even larger scales and found that the Aquila supershell expansion is a plausible candidate to have swept up the material to form the W 48 complex, since the velocity of the shell matches the LSR velocities of the W 48A-E H II regions, and the age gradient of the W 48 H II regions is roughly aligned with the direction of the expansion of the shell.

ACKNOWLEDGEMENTS

The authors thank the anonymous referee for his/her detailed comments which lead to a significant improvement of the manuscript. Furthermore, the authors are very grateful to Gemma Busquet, Miguel Pereira-Santaella and Scige J. Liu. The staff of both the BIMA and IRAM 30 m telescopes are acknowledged for their support during the observations. KLJR acknowledges funding by the Agenzia Spaziale Italiana (ASI) under contract number I/005/11/0. DP is funded through the Operational Program 'Education and Lifelong Learning'Ó and is co-financed by the European Union (European Social Fund) and Greek national funds. Part of this work was supported by the French National Agency for Research (ANR) project 'PROBeS', number ANR-08-BLAN-0241.

SPIRE has been developed by a consortium of institutes led by Cardiff University (UK) and including Univ. Lethbridge (Canada); NAOC (China); CEA, LAM (France); IFSI, Univ. Padua (Italy); IAC (Spain); Stockholm Observatory (Sweden); Imperial College London, RAL, UCL-MSSL, UKATC, Univ. Sussex (UK); and Caltech, JPL, NHSC, Univ. Colorado (USA). This development has been supported by national funding agencies: CSA (Canada); NAOC (China); CEA, CNES, CNRS (France); ASI (Italy); MCINN (Spain); SNSB (Sweden); STFC (UK); and NASA (USA). PACS has been developed by a consortium of institutes led by MPE (Germany) and including UVIE (Austria); KU Leuven, CSL, IMEC (Belgium); CEA, LAM (France); MPIA (Germany); INAF-IFSI/OAA/OAP/OAT, LENS, SISSA (Italy); IAC (Spain). This development has been supported by the funding agencies BMVIT (Austria), ESA-PRODEX (Belgium), CEA/CNES (France), DLR (Germany), ASI/INAF (Italy) and CICYT/MCYT (Spain). The BIMA array was operated with support from the National Science Foundation under grants AST-9981308 to UC Berkeley, AST-9981363 to U. Illinois, and AST-9981289 to U. Maryland. The James Clerk Maxwell Telescope is operated by the Joint Astronomy Centre on behalf of the Science and Technology Facilities Council of the United Kingdom, the Netherlands Organisation for Scientific Research and the National Research Council of Canada. This research has made use of the SIMBAD data base and the VizieR service, operated at CDS, Strasbourg, France.

REFERENCES

Akeson R. L., Carlstrom J. E., 1996, ApJ, 470, 528
Araya E., Hofner P., Kurtz S., Bronfman L., DeDeo S., 2005, ApJS, 157, 279
Arce H. G., Borkin M. A., Goodman A. A., Pineda J. E., Beaumont C. N., 2011, ApJ, 742, 105
Arthur S. J., Hoare M. G., 2006, ApJS, 165, 283
Barrett A. H., Ho P. T. P., Myers P. C., 1977, ApJ, 211, L39
Beltrán M. T., Brand J., Cesaroni R., Fontani F., Pezzuto S., Testi L., Molinari S., 2006, A&A, 447, 221
Bergin E. A., Tafalla M., 2007, ARA&A, 45, 339
Bernard J.-P. et al., 2010, A&A, 518, L88
Beuther H., Schilke P., Menten K. M., Motte F., Sridharan T. K., Wyrowski F., 2002, ApJ, 566, 945
Blaauw A., 1964, ARA&A, 2, 213
Bontemps S., Motte F., Csengeri T., Schneider N., 2010, A&A, 524, A18
Breen S. L., Ellingsen S. P., Caswell J. L., Lewis B. E., 2010, MNRAS, 401, 2219
Breen S. L., Ellingsen S. P., Contreras Y., Green J. A., Caswell J. L., Stevens J. B., Dawson J. R., Voronkov M. A., 2013, MNRAS, 435, 524
Cambrésy L., Marton G., Feher O., Tóth L. V., Schneider N., 2013, A&A, 557, A29
Carey S. J. et al., 2009, PASP, 121, 76
Caswell J. L., 2001, MNRAS, 326, 805
Cavanagh B., Jenness T., Economou F., Currie M. J., 2008, Astron. Nachr., 329, 295
Cazaux S., Tielens A. G. G. M., Ceccarelli C., Castets A., Wakelam V., Caux E., Parise B., Teyssier D., 2003, ApJ, 593, L51
Charnley S. B., Tielens A. G. G. M., Millar T. J., 1992, ApJ, 399, L71
Churchwell E., Walmsley C. M., Wood D. O. S., 1992, A&A, 253, 541
Codella C., Moscadelli L., 2000, A&A, 362, 723
Condon J. J., Cotton W. D., Greisen E. W., Yin Q. F., Perley R. A., Taylor G. B., Broderick J. J., 1998, AJ, 115, 1693
Csengeri T., Bontemps S., Schneider N., Motte F., Gueth F., Hora J. L., 2011, ApJ, 740, L5
Curran R. L., Chrysostomou A., Collett J. L., Jenness T., Aitken D. K., 2004, A&A, 421, 195
Cyganowski C. J., Reid M. J., Fish V. L., Ho P. T. P., 2003, ApJ, 596, 344
Dale J. E., Bonnell I., 2011, MNRAS, 414, 321
Dale J. E., Bonnell I. A., 2012, MNRAS, 422, 1352
Deharveng L., Zavagno A., Caplan J., 2005, A&A, 433, 565
Deharveng L. et al., 2012, A&A, 546, A74
Di Francesco J., Johnstone D., Kirk H., MacKenzie T., Ledwosinska E., 2008, ApJS, 175, 277
Du F., Yang J., 2008, ApJ, 686, 384
Duarte-Cabral A., Bontemps S., Motte F., Hennemann M., Schneider N., André Ph., 2013, A&A, 558, A125
Elia D. et al., 2010, A&A, 518, L97
Elia D. et al., 2013, ApJ, 772, 45
Elmegreen B. G., Lada C. J., 1977, ApJ, 214, 725
Fallscheer C. et al., 2013, ApJ, 773, 102
Fontani F., Cesaroni R., Furuya R. S., 2010, A&A, 517, A56
Giannini T. et al., 2012, A&A, 539, A156
Goddi C., Moscadelli L., Sanna A., 2011, A&A, 535, L8
Goedhart S., Gaylard M. J., van der Walt D. J., 2004, MNRAS, 355, 553
Goldsmith P. F., Langer W. D., 1999, ApJ, 517, 209
Greisen E. W., 2003, in Heck A., ed., Astrophysics and Space Science Library, Vol. 285, Information Handling in Astronomy – Historical Vistas. Kluwer, Dordrecht, p. 109
Griffin M. J. et al., 2010, A&A, 518, L3

Hachisuka K. et al., 2006, ApJ, 645, 337
Hennemann M. et al., 2010, A&A, 518, L84
Hennemann M. et al., 2012, A&A, 543, L3
Henning T., 2008, in Beuther H., Linz H., Henning T., eds, ASP Conf. Ser. Vol. 387, Massive Star Formation: Observations Confront Theory. Astron. Soc. Pac., San Francisco, p. 452
Hildebrand R. H., 1983, QJRAS, 24, 267
Hill T. et al., 2011, A&A, 533, A94
Hill T. et al., 2012, A&A, 542, A114
Hofner P., Churchwell E., 1996, A&AS, 120, 283
Holland W. S. et al., 1999, MNRAS, 303, 659
Jenness T., Berry D., Chapin E., Economou F., Gibb A., Scott D., 2011, in Evans I. N., Accomazzi A., Mink D. J., Rots A. H., eds, ASP Conf. Ser. Vol. 442, Astronomical Data Analysis Software and Systems XX. Astron. Soc. Pac., San Francisco, p. 281
Juvela M. et al., 2011, A&A, 527, A111
Kauffmann J., Bertoldi F., Bourke T. L., Evans N. J., II, Lee C. W., 2008, A&A, 487, 993
Kelly B. C., Shetty R., Stutz A. M., Kauffmann J., Goodman A. A., Launhardt R., 2012, ApJ, 752, 55
Kreysa E. et al., 1998, in Phillips T. G., ed. Proc. SPIE Conf. Ser. Vol. 3357, Advanced Technology MMW, Radio, and Terahertz Telescopes. SPIE, Bellingham, p. 319
Kurtz S., Franco J., 2002, in Henney W. J., Franco J., Martos M., eds, Rev. Mex. Astron. Astrofis. Conf. Vol. 12, Ionized Gaseous Nebulae. Universidad Nacional Autonoma de Mexico, Mexico City, p. 16
Kurtz S., Churchwell E., Wood D. O. S., 1994, ApJS, 91, 659
Kutner M. L., Ulich B. L., 1981, ApJ, 250, 341
López-Sepulcre A., Codella C., Cesaroni R., Marcelino N., Walmsley C. M., 2009, A&A, 499, 811
Maciejewski W., Murphy E. M., Lockman F. J., Savage B. D., 1996, ApJ, 469, 238
Martins F., Schaerer D., Hillier D. J., 2005, A&A, 436, 1049
Matsuyanagi I., Itoh Y., Sugitani K., Oasa Y., Mukai T., Tamura M., 2006, PASJ, 58, L29
Menten K. M., 1991, ApJ, 380, L75
Miettinen O., Harju J., Haikala L. K., Juvela M., 2012, A&A, 538, A137
Minier V., Booth R. S., Conway J. E., 2000, A&A, 362, 1093
Minier V., Ellingsen S. P., Norris R. P., Booth R. S., 2003, A&A, 403, 1095
Minier V. et al., 2013, A&A, 550, A50
Molinari S., Brand J., Cesaroni R., Palla F., 1996, A&A, 308, 573
Molinari S., Brand J., Cesaroni R., Palla F., Palumbo G. G. C., 1998, A&A, 336, 339
Molinari S., Brand J., Cesaroni R., Palla F., 2000, A&A, 355, 617
Molinari S., Pezzuto S., Cesaroni R., Brand J., Faustini F., Testi L., 2008, A&A, 481, 345
Molinari S., Schisano E., Faustini F., Pestalozzi M., di Giorgio A. M., Liu S., 2011, A&A, 530, A133
Moscadelli L., Sanna A., Goddi C., 2011, A&A, 536, A38
Motte F., Bontemps S., Schilke P., Schneider N., Menten K. M., Broguière D., 2007, A&A, 476, 1243
Motte F. et al., 2010, A&A, 518, L77
Nguyen Luong Q. et al., 2011, A&A, 535, A76
Ogura K., Chauhan N., Pandey A. K., Bhatt B. C., Ojha D., Itoh Y., 2007, PASJ, 59, 199
Olmi L., Cesaroni R., Walmsley C. M., 1993, A&A, 276, 489
Olmi L., Cesaroni R., Neri R., Walmsley C. M., 1996, A&A, 315, 565
Onello J. S., Phillips J. A., Benaglia P., Goss W. M., Terzian Y., 1994, ApJ, 426, 249
Ott S., 2010, in Mizumoto Y., Morita K.-I., Ohishi M., eds, ASP Conf. Ser. Vol. 434, Astronomical Data Analysis Software and Systems XIX. Astron. Soc. Pac., San Francisco, p. 139
Palau A., Estalella R., Girart J. M., Ho P. T. P., Zhang Q., Beuther H., 2007, A&A, 465, 219
Palau A., Sánchez-Monge Á., Busquet G., Estalella R., Zhang Q., Ho P. T. P., Beltrán M. T., Beuther H., 2010, A&A, 510, A5
Palau A. et al., 2013, ApJ, 762, 120
Palla F., Brand J., Comoretto G., Felli M., Cesaroni R., 1991, A&A, 246, 249
Panagia N., 1973, AJ, 78, 929
Pety J., 2005, in Casoli F., Contini T., Hameury J. M., Pagani L., eds, SF2A-2005: Semaine de l'Astrophysique Francaise, p. 721
Phillips J. P. et al., 1988, A&A, 190, 289
Piazzo L., Ikhenaode D., Natoli P., Pestalozzi M., Piacentini F., Traficante A., 2012, IEEE Trans. Image Process., 21, 3687
Pickett H. M., Poynter R. L., Cohen E. A., Delitsky M. L., Pearson J. C., Müller H. S. P., 1998, J. Quant. Spectrosc. Radiat. Transfer, 60, 883
Pilbratt G. L. et al., 2010, A&A, 518, L1
Pillai T., Wyrowski F., Carey S. J., Menten K. M., 2006, A&A, 450, 569
Pillai T., Kauffmann J., Wyrowski F., Hatchell J., Gibb A. G., Thompson M. A., 2011, A&A, 530, A118
Poglitsch A. et al., 2010, A&A, 518, L2
Purcell C. R. et al., 2006, MNRAS, 367, 553
Qiu K. et al., 2008, ApJ, 685, 1005
Reid M. J., Schneps M. H., Moran J. M., Gwinn C. R., Genzel R., Downes D., Roennaeng B., 1988, ApJ, 330, 809
Remijan A., Sutton E. C., Snyder L. E., Friedel D. N., Liu S.-Y., Pei C.-C., 2004, ApJ, 606, 917
Rivera-Ingraham A. et al., 2013, ApJ, 766, 85
Roshi D. A., Goss W. M., Anantharamaiah K. R., Jeyakumar S., 2005, ApJ, 626, 253
Roussel H., 2013, PASP, 125, 1126
Rygl K. L. J., Wyrowski F., Schuller F., Menten K. M., 2010, A&A, 515, A42
Rygl K. L. J., Wyrowski F., Schuller F., Menten K. M., 2013, A&A, 549, A5
Sadavoy S. I. et al., 2013, ApJ, 767, 126
Saraceno P., Andre P., Ceccarelli C., Griffin M., Molinari S., 1996, A&A, 309, 827
Sault R. J., Teuben P. J., Wright M. C. H., 1995, in Shaw R. A., Payne H. E., Hayes J. J. E., eds, ASP Conf. Ser. Vol. 77, Astronomical Data Analysis Software and Systems IV. Astron. Soc. Pac., San Francisco, p. 433
Schneider N. et al., 2010, A&A, 518, L83
Schneider N. et al., 2012, A&A, 542, L18
Shepherd D. S., Churchwell E., 1996, ApJ, 472, 225
Thompson M. A., White G. J., Morgan L. K., Miao J., Fridlund C. V. M., Huldtgren-White M., 2004, A&A, 414, 1017
Torrelles J. M., Ho P. T. P., Rodriguez L. F., Canto J., 1989, ApJ, 343, 222
Traficante A. et al., 2011, MNRAS, 416, 2932
Tremblin P. et al., 2014, arXiv:1401.7333
Turner B. E., 1991, ApJS, 76, 617
Val'tts I. E., Lyubchenko S. Y., 2002, in Migenes V., Reid M. J., eds, Proc. IAU Symp. 206, Cosmic Masers: From Proto-Stars to Black Holes. Astron. Soc. Pac., San Francisco, p. 167
Val'tts I. E., Dzura A. M., Kalenskii S. V., Slysh V. I., Booth R. S., Winnberg A., 1995, A&A, 294, 825
van der Tak F. F. S., van Dishoeck E. F., Caselli P., 2000, A&A, 361, 327
Walsh A. J., Burton M. G., Hyland A. R., Robinson G., 1998, MNRAS, 301, 640
Wang K., Zhang Q., Wu Y., Zhang H., 2011, ApJ, 735, 64
White G. J., Lefloch B., Fridlund C. V. M., Aspin C. A., Dahmen G., Minchin N. R., Huldtgren M., 1997, A&A, 323, 931
Whitworth A. P., Bhattal A. S., Chapman S. J., Disney M. J., Turner J. A., 1994, MNRAS, 268, 291
Wood D. O. S., Churchwell E., 1989, ApJS, 69, 831
Wright E. L. et al., 2010, AJ, 140, 1868
Xie T., Mundy L. G., Vogel S. N., Hofner P., 1996, ApJ, 473, L131
Ysard N. et al., 2013, A&A, 559, A133
Zavagno A. et al., 2010a, A&A, 518, L81
Zavagno A. et al., 2010b, A&A, 518, L101
Zhang Q., Hunter T. R., Sridharan T. K., Ho P. T. P., 2002, ApJ, 566, 982
Zhang B., Zheng X. W., Reid M. J., Menten K. M., Xu Y., Moscadelli L., Brunthaler A., 2009a, ApJ, 693, 419
Zhang Q., Wang Y., Pillai T., Rathborne J., 2009b, ApJ, 696, 268

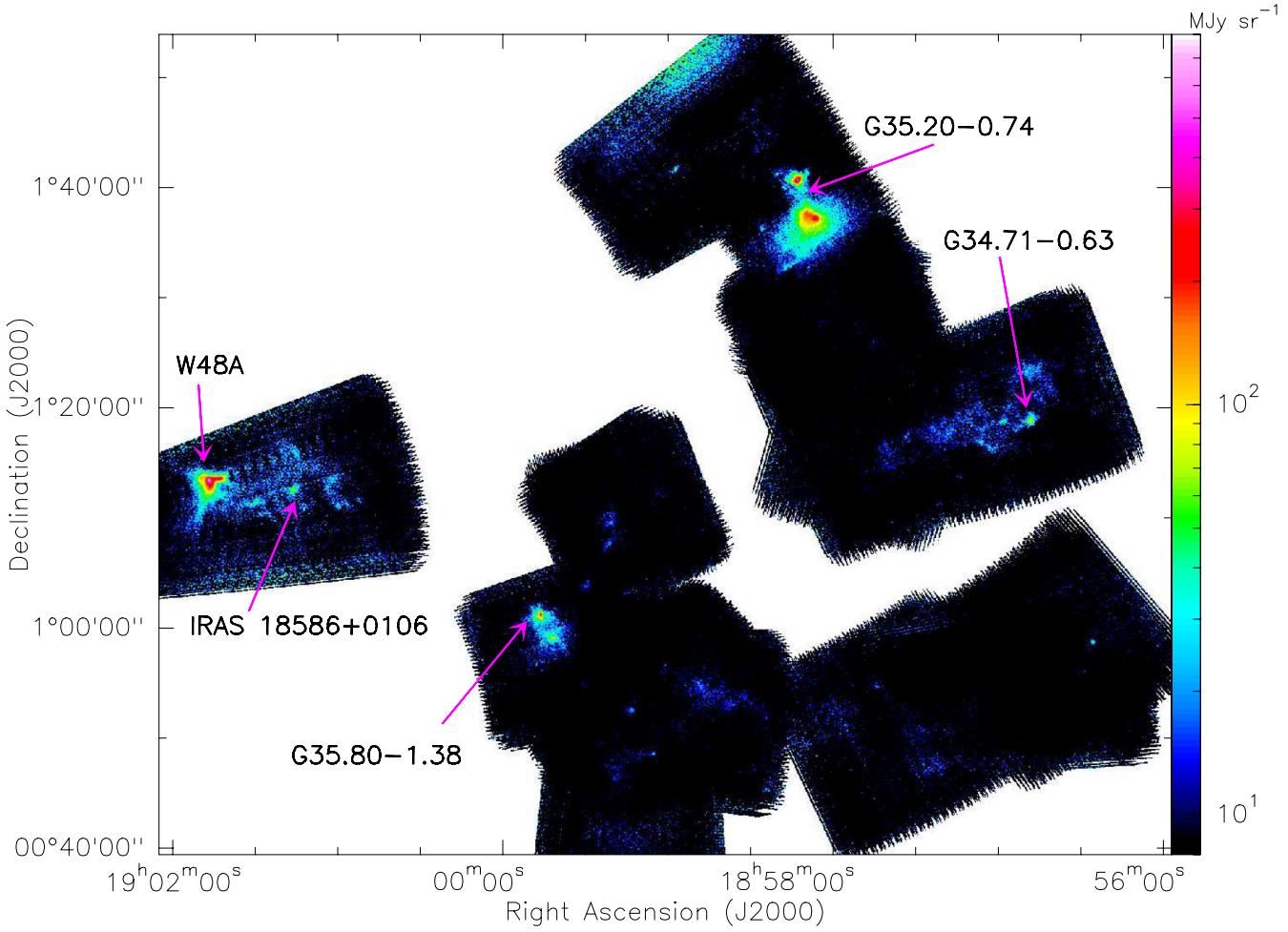

Figure A1. Full MAMBO 1.3 mm continuum map. Apart from W 48A and IRAS 18586, other mm-bright star-forming regions in the field are indicated.

APPENDIX A: MAMBO 1.3 MM MAP

The 1.3 mm MAMBO data of W 48A shown in Fig. 2 were part of a larger map presented in Fig. A1. Observational details are given in Section 2.3 and Table 1.

APPENDIX B: DISTRIBUTION OF 107 GHZ METHANOL MASERS

The spectra of the 107 GHz masers compared to the 12.2 GHz (M. Gaylard, private communication) and 6.7 GHz masers (Goedhart, Gaylard & van der Walt 2004) are shown in Fig. B1. While the 6.7 and 12.2 GHz masers share the same velocity range of 39.5–46 km s^{-1}, the 107 GHz masers show emission out to 48 km s^{-1}, indicating that various transitions probe similar but not the same physical conditions. The relative intensities of individual maser features are different at each transition, with the redshifted features brighter at 107 GHz (see also the work of Val'tts & Lyubchenko 2002).

The 107 GHz methanol maser spots were detected across a velocity range of ∼8 km s^{-1} (see Fig. B1) and appear to be unresolved in the data cubes generated. We obtained the positions of the methanol maser spots by fitting two-dimensional Gaussians to the data cube from the (highest resolution) BIMA A-array data. The beam size from A-array data alone is 0.57 arcsec × 0.24 arcsec (Table 1) but two-dimensional Gaussian fitting can find the centre of the maser spot to much higher accuracy, ∼0.01 arcsec (33 au). The spatial and velocity distribution of the 107 GHz methanol masers is shown in Fig. B2.

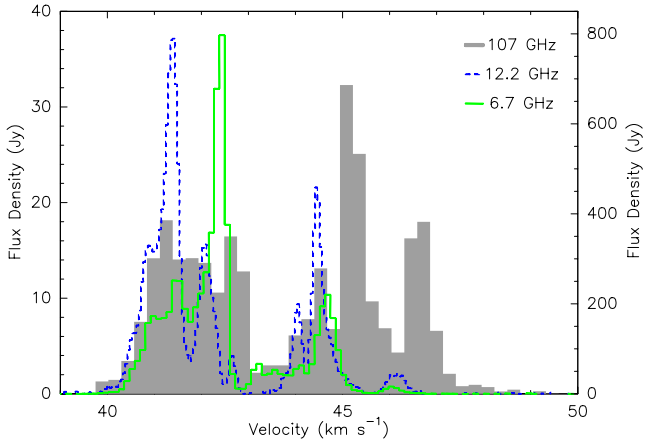

Figure B1. Spectra of 107 GHz (grey histogram), 12.2 GHz (dashed blue) and 6.7 GHz (green) methanol masers towards clump H-2 in W 48A. The left *y*-axis is for the 107 and 12.2 GHz transitions, while the right *y*-axis belongs to the 6.7 GHz methanol maser.

Methanol maser kinematics can trace the small-scale gas motions near the protostar, such as envelope expansion or a rotating disc

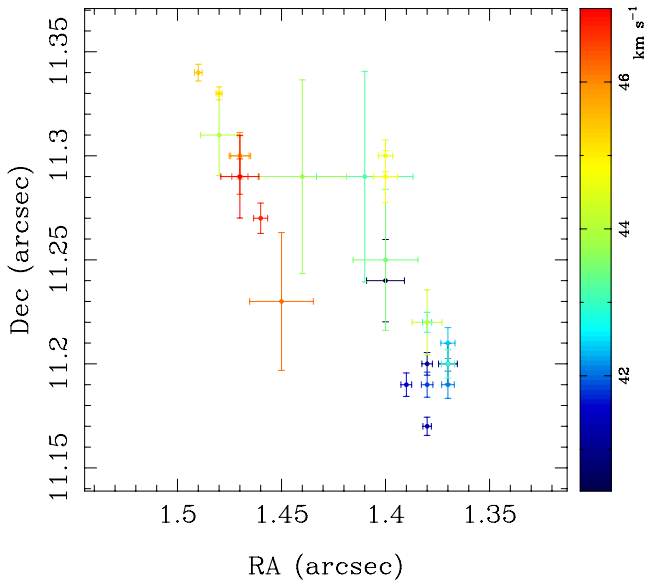

Figure B2. 107 GHz methanol maser map obtained through Gaussian fitting. Weaker features have higher positional uncertainties. Axes give the offset in arcseconds with respect to the pointing centre $19^{h}\,01^{m}\,45\overset{s}{.}448$ $+01^{\circ}\,13'\,21\overset{''}{.}493$ (J2000).

(Moscadelli, Sanna & Goddi 2011). AFGL 5142 is an example of a high-mass protostar where the 3D kinematics of methanol masers seem to be emanating from a rotation disc (Goddi, Moscadelli & Sanna 2011). The general morphology and angular distribution of the 107 GHz masers is similar to that found for the 6.7 and 12.2 GHz masers by Minier et al. (2000): spots belonging to the redshifted group in the north-east and spots belonging to the blueshifted group in the south-west. However, a one-to-one correspondence of spots in the different transitions is not apparent. The 107 GHz emission appears to be coming from a smaller area than seen in Minier et al. (2000): ∼0.21 arcsec compared to the ∼0.43 arcsec. The 107 GHz masers show a tighter correlation in position and velocities than the 6.7 and 12.2 GHz masers. We find a correlation coefficient of 0.86 by performing a linear fit to the 107 GHz maser distribution. If we assume Keplerian rotation and a distance of 3.27 kpc (Zhang et al. 2009a), the mass enclosed in 0.21 arcsec (0.003 pc or 685 au) is derived to be $2.2\cos^{-2}(i)\,M_{\odot}$. Furthermore, if we interpret the spatial distribution of 6.7 and 12.2 GHz masers in Minier et al. (2000) as due to the inclination i of the disc, we obtain an inclination of 30°. Applying this inclination, the enclosed mass increases to $3\,M_{\odot}$, which about a factor of 2 lower than the mass obtained by Minier et al. (2000) enclosed in 1300 au. Class II methanol masers, to which the 6.7, 12.2 and 107 GHz masers belong, are associated with *high-mass* star formation (Menten 1991; Minier et al. 2003; Breen et al. 2013). Our derived mass of $3\,M_{\odot}$ is unlikely to form a high-mass star, indicating that the 107 GHz masers do not allow a mass calculation, because, for example, they do not trace the entire disc, as also suggested recently in Breen et al. (2013).

APPENDIX C: DISTRIBUTION OF $NH_3(2,2)/NH_3(1,1)$ MAIN BEAM TEMPERATURES

The ratio of the $NH_3(2,2)$ to $NH_3(1,1)$ main beam temperature is a sign of increasing kinetic temperature (Torrelles et al. 1989; Zhang et al. 2002), and can be used to trace heating sources. Fig. C1 shows the distribution of this ratio based on the VLA cubes. Near clump H-2 the ratio is high. This sign of heating is consistent with the presence of a PDR as seen in previous studies of PDRs near H II regions (e.g. Palau et al. 2007). Note that the gas near clump H-1 has a low ratio, which indicates that this gas is cold, and hence in front of the UC H II region – this agrees with the NH_3 absorption seen at this location (see Section 3.4).

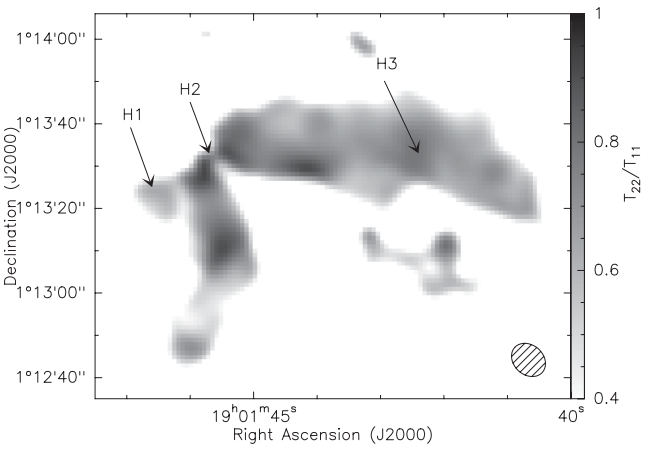

Figure C1. Ratio of $NH_3(2,2)$ to $NH_3(1,1)$ main beam temperatures. The beam is shown in the bottom-right corner.

APPENDIX D: IRAS 18586+0106

IRAS 18586+0106 originated from the *IRAS*-colour-selected list of *low* sources by Palla et al. (1991), which was consequently studied in NH_3, centimetre and submillimetre emission (Molinari et al. 1996, 1998, 2000; Beltrán et al. 2006). The object was found to have weak NH_3 and submillimetre emission, and no radio emission (the radio emission was found to be uncorrelated with the *IRAS* source). The *IRAS* resolutions at the various wavelengths [for example, the point spread function (PSF) at 60 μm was ∼2 arcmin × 5 arcmin] are nowadays surpassed by those of *Herschel* (∼6 arcsec at 70 μm). Fig. D1 shows the 70 and 250 μm *Herschel* and 1.2 mm MAMBO maps of the *IRAS* source. Note that the image is completely within the *IRAS* PSF at 60 μm, and that two clear clumps, marked as A and B, are present. Of these, source A (which coincides with the centre of the *IRAS* source) is brighter at shorter wavelengths indicating a later evolutionary stage than that of source B, which is more luminous in the far-infrared to submillimetre. Performing the source extraction and SED fitting (Fig. D2), as described in Section 3.1.1, we find that source A has a temperature of 35 K, an envelope mass of $70\,M_{\odot}$ and a bolometric luminosity of 2140 $L_{\odot}$ (including the *WISE* data from Wright et al. 2010). Source B (SED not shown) has a temperatures of 17 K, a mass of $300\,M_{\odot}$ and a bolometric luminosity of $470\,L_{\rm bol}$.

Source A is located between the evolutionary tracks of the 6.2 and $8.0\,M_{\odot}$ stars in the L/M diagram (Molinari et al. 2008), suggesting that it will form an intermediate- to high-mass star and that it has an age of $\sim 4.5 \times 10^5$ yr. Source B lies on the $13.5\,M_{\odot}$ track and its combination of estimated mass and luminosity gives an age of 3×10^5 yr.

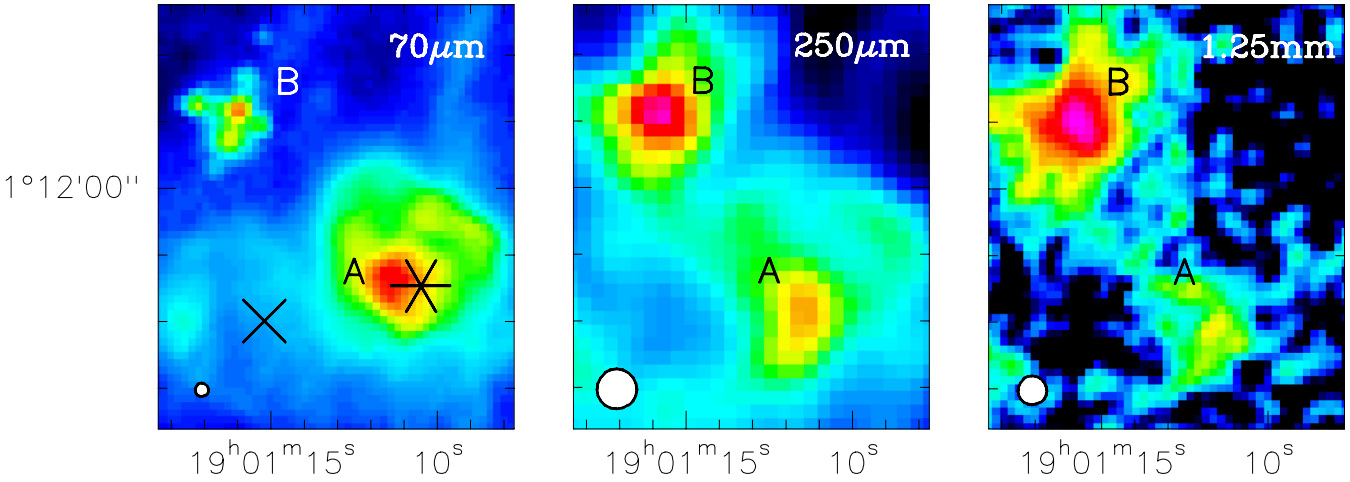

Figure D1. *Herschel* 70 μm, 250 μm and MAMBO 1.2 mm maps of IRAS 18586+0106 revealing two clear clumps, A and B. The position of the *IRAS* source is marked by a star. The radio source (Molinari et al. 1998) is marked by a cross. The beam FWHM is given in the bottom-left corner.

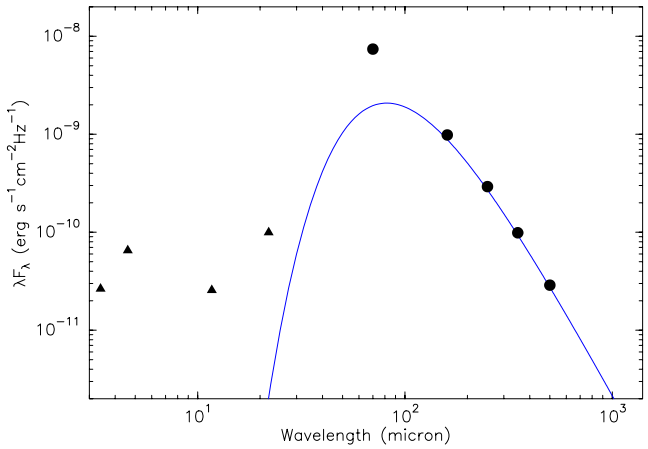

Figure D2. Best modified blackbody fit to the IRAS 18586+0106 SED. *WISE* data points (Wright et al. 2010) are marked with triangles and *Herschel* data points with filled dots.

[1]*Istituto di Astrofisica e Planetologia Spaziali (INAF-IAPS), Via del Fosso del Cavaliere 100, I-00133 Roma, Italy*
[2]*European Space Research and Technology Centre (ESA-ESTEC), Keplerlaan 1, PO Box 299, NL-2200 AG Noordwijk, the Netherlands*
[3]*SKA South Africa, 3rd Floor, The Park, Park Rd, Pinelands 7405, South Africa*
[4]*Max-Planck-Institut für Radioastronomie, Auf dem Hügel 69, D-53121 Bonn, Germany*
[5]*Hartebeesthoek Radio Astronomy Observatory, PO Box 443, Krugersdorp 1740, South Africa*
[6]*Department of Astrophysics, Astronomy and Mechanics, Faculty of Physics, University of Athens, Panepistimiopolis, GR-15784 Zografos, Athens, Greece*
[7]*Laboratoire AIM Paris-Saclay, CEA/IRFU CNRS/INSU Université Paris Diderot, F-91191 Gif-sur-Yvette, France*
[8]*Canadian Institute for Theoretical Astrophysics (CITA), University of Toronto, 60 St. George Street, Toronto, ON M5S 3H8, Canada*
[9]*Department of Physics & Astronomy, University of Victoria, PO Box 355, STN CSC, Victoria, BC V8W 3P6, Canada*
[10]*National Research Council Canada, 5071 West Saanich Road, Victoria, BC V9E 2E7, Canada*
[11]*Department of Physics and Astronomy, University of British Columbia, 6224 Agricultural Road, Vancouver, BC V6T 1Z1, Canada*
[12]*Joint ALMA Observatory, Alonso de Cordova 3107, Vitacura 763-0355, Santiago, Chile*
[13]*Institut d'Astrophysique Spatiale, UMR8617, CNRS/Université Paris-Sud 11, F-91405 Orsay, France*
[14]*ESA/ESAC, PO Box 78, E-28691 Villanueva de la Canada, Madrid, Spain*
[15]*Université de Toulouse, UPS-OMP, IRAP, F-31028 Toulouse, France*
[16]*CNRS, IRAP, 9 Av. colonel Roche, BP 44346, F-31028 Toulouse cedex 4, France*
[17]*Infrared Processing and Analysis Center, Institute of Technology, Pasadena, CA 91125, USA*
[18]*OASU/LAB-UMR5804, CNRS, Université Bordeaux 1, F-33270 Floirac, France*
[19]*Jeremiah Horrocks Institute, University of Central Lancashire, Preston, Lancashire PR1 2HE, UK*
[20]*Space Science and Technology Department, STFC Rutherford Appleton Laboratory, Chilton, Didcot, Oxfordshire OX11 0QX, UK*
[21]*Department of Physics and Astronomy, The Open University, Walton Hall, Milton Keynes MK7 6AA, UK*

This paper has been typeset from a TEX/LATEX file prepared by the author.